Glacier changes and surges over Xinqingfeng and Malan Ice Caps in the inner Tibetan Plateau since 1970 derived from Remote Sensing Data

Zhen Zhang[1*], Shiyin Liu[2,3*], Zongli Jiang[4], Donghui Shangguan[3], Junfeng Wei[4], Wanqin Guo[3], Junli Xu[5], Yong Zhang[4] and Danni Huang[1]

[1]School of Geomatics, Anhui University of Science and Technology, Huainan, 232001, China

[2]Institute of International Rivers and Eco−Security, Yunnan University, Kunming, 650500, China

[3]State Key Laboratory of Cryospheric Science, Northwest Institute of Eco−Environment and Resources, Chinese Academy of Sciences, Lanzhou, 730000, China

[4]School of Resource Environment and Safety Engineering, Hunan University of Science and Technology, Xiangtan, 411201, China

[5]College of Urban and Environmental Sciences, Yancheng Teachers University, Yancheng, 224002, China

Correspondence to: Zhen Zhang (zhangzhen@aust.edu.cn) and Shiyin Liu (shiyin.liu@ynu.edu.cn)

Abstract. The inner Tibetan Plateau region is a glacierised region where glaciers show heterogeneous change. The Xinqingfeng and Malan ice caps are located in this region and a transition zone exists with shifting influences between the westerlies and Indian summer monsoon. However, information regarding the detailed glacier area and mass changes in this region prior to 2000 are scarce. In the present study, we present an integrated view of the glacier area and its mass changes for Mt. Xinqingfeng and Mt. Malan as derived from topographic maps, Landsat, ASTER, SRTM DEM, and TerraSAR-X/TanDEM-X from1970 to 2012 and from1970 to 2018, respectively. Our results showed that the glaciers experienced a slight shrinkage in area by 0.09 ±0.03% a^{-1} from 1970 to 2018 with a median mass loss rate of 0.22 ± 0.17 m w.e. a^{-1} and 0.29 ± 0.17 m w.e. a^{-1} between 1999 and 2012 at Mt. Xinqingfeng and Mt. Malan, respectively. The glaciers of Mt. Malan had a total mass loss of 0.19 ± 0.14 m w.e. a^{-1} during 1970–1999. A minimum of seven glaciers at Mt. Xinqingfeng and Mt. Malan showed heterogeneous variations with either surging or advancing during the observation period. Among them, the West Monuomaha Glacier, Monuomaha Glacier, and Zu Glacier were identified as surging glaciers, and the others may also be surging glaciers, although more evidence is required. These glaciers showed a long active period and comparatively low velocities, therefore, thermal controls are important for surge initiation and recession.

1 Introduction

Glaciers in the High Mountains Asia (HMA) are the headwater sources for many rivers and lakes. Thus, HMA is also known as the 'Asia Water Tower'(Immerzeel et al., 2010). During the recent warming climate, many sub-regions of the HMA, such as the Himalayas, Nyainqentanglha, and Tien Shan have experienced glacier mass loss (Brun et al., 2017; Farinotti et al., 2015; Kääb et al., 2012; Kääb et al., 2015; Wu et al., 2018). However, glaciers in Pamir, Karakoram and West Kunlun have,

on average, been in near balance or have shown a mass gain, which is attributed to the strengthening westerlies in recent years (Bao et al., 2015; Bolch et al., 2017; Gardelle et al., 2012b; Gardelle et al., 2013; Holzer et al., 2015; Kääb et al., 2015; Lin et al., 2017; Zhang et al., 2016). The very large inner Tibetan Plateau (ITP) region is located in the transition zone of the atmospheric circulation systems of monsoon and westerlies and is dominated more by continental climate conditions, with glaciers at ITP showing heterogeneous variabtions. Glaciers found in the eastern and southern ITP have shown significant retreating and mass loss, which is similar to that seen at the Himalayas and Nyainqentanglha and is influenced by the weakening Indian monsoon (Brun et al., 2017; Yao et al., 2012). However, glaciers in the western ITP have shown near stable or slight mass gain, which accords with West Kunlun and is influenced by the strengthening westerlies (Brun et al., 2017; Yao et al., 2012). According to the results of glacier elevation changes and mass balance for HMA (2000–2016) reported by Brun et al. (2017), glaciers at the north side of 32° N at ITP showed a clear east-west direction difference, those at the west side of 90° E showed near stable or slight mass gain, and on the east side showed significant retreating and mass loss. Four main clusters of glaciers (Kangzhag Ri, Purogangri, Xinqingfeng and Malan Ice Caps (collective known as XM) and Geladandong) are distributed near 90 °E. Among them, Kangzhag Ri and Purogangri are located at the west side of 90 °E, and XM and Geladandong are located at the east side of 90 °E. The latitude of Kangzhag Ri and XM are close, and the latitude of Purogangri and Geladandong are close. Several studies have reported that glaciers at Kangzhag Ri and Purogangri experienced near stable mass (-0.04 ± 0.02 m w.e. a^{-1}) and mass gain ($+0.16 \pm 0.02$ m w.e. a^{-1}) during 1999-2012, respectively (Neckel et al., 2013; Zhang and Liu, 2018). However, glaciers at Kangzhag Ri experienced a negative mass balance (-0.34 ± 0.01 m w.e. a^{-1}) during 1970–1999 and glaciers at Geladandong experienced a negative mass balance (-0.21 ± 0.16 m w.e. a^{-1}) during 1969–1999, and accelerated glacier mass loss (-0.33 ± 0.38 m w.e. a^{-1}) during 1999–2015 (Chen et al., 2017). Therefore, how glaciers change at XM and whether these changes have been consistent with those of the glaciers at Kangzhag Ri and Purogangri is still an unresolved issue. There is little detailed analysis regarding the status of XM glaciers located to the east of Kangzhag Ri with limited knowledge regarding the glacier mass change before 1999. Glacier surging can cause hazards, such as floods and associated impacts on downstream areas (Kotlyakov et al., 2004; Motyka and Truffer, 2007). HMA is one of the major 'superclusters' of glacier surge (Sevestre and Benn, 2015). However, there have been sporadic reports of surging glaciers for the ITP, such as Aru Co, Ányêmaqên, Ulugh Muztagh, Namjagbarwa, and Geladandong (Guo et al., 2013; Jiang et al., 2018; Xu et al., 2018; Zhang, 1983; Zhang et al., 2018). Consequently, more attention is urgently required to investigate the recent glacier changes at XM.

Zhou et al. (2019) reported that Xinqingfeng and Malan had mass budgets of -0.21 ± 0.10 m w.e. a^{-1} and -0.22 ± 0.10 m w.e. a^{-1}, respectively, between 2000 and 2016 from optical stereo images (SPOT-6/7) and SRTM. Geodetic mass balance measurements by optical stereo data produces good results on rough surfaces, such as debris-coverd glacier surfaces, however, such measurements are difficult where there are clouds, shadow, and snow cover due to high saturation or low

contrast alterations. As Interferometric synthetic-aperture radar (InSAR) is independent of visible structures and contrast of the glacier surface, therefore, it performs well in accumulation areas such as the snow cover of glaciers. SAR can perform well at all weather conditions. The single pass configuration of TerraSAR-X and TanDEM-X ensures a high coherence on glaciers which is advantageous compared to repeat-pass InSAR. The comparison between TerraSAR-X /TanDEM-X and SRTM has been employed for estimating the mass balance of glaciers after 1999 in the HMA (Lin et al., 2017; Neckel et al., 2013; Wu et al., 2018). Few optical stereo data exist before 2000, which has constrainted the research for glacier mass changes before this time. The historical national topographic maps, which are strictly based on the national specialised standard, have a high accuracy and provide a fine depiction of glacier surface topography, and have been widely used for glaciological purposes, especially for glacier mass changes before 2000 (Wei et al., 2015a; Wei et al., 2015b; Zhang et al., 2016). In the present study, we used topographic maps, Landsat, ASTER, SRTM DEM, and TerraSAR-X/TanDEM-X to assess the glacier area and mass changes since 1970 for Mt. Xinqingfeng and Mt. Malan in the ITP. The study aimed to fill the knowledge gap of detailed studies in this region and to improve the knowledge of the glacier change anomaly, such as advancing and surging.

2 Study area

Xinqingfeng (also called Buka Daban Peak, see Fig. 1) is located in the central Hoh Xil region of the Kunlun Mountain. It is a small ice cap that developed on the planation surface of Kunlun Mountain. The highest elevation is 6860 m above sea level (a.s.l.). According to the second Chinese glacier inventory (CGI), Xinqingfeng contained 77 glaciers with a total area of 425.4 km^2 in 2006. The glaciers are distributed around the ice cap with short tongues and with an average terminus altitude of approximately 5056 m. The largest glacier is located on the southeastern slope called Monuomaha Glacier (or Xinqingfeng Glacier, Glacier No. 4), with an area of 83.9 km^2, and the second largest glacier is located on the northwestern slope called the West Monuomaha Glacier (Glacier No.2), with an area of 69.0 km^2.

The Malan Ice Caps (Fig. 1) are located on the southwest side of Xinqingfeng, where the highest elevation is 6,056 m a.s.l. According to the second CGI, the Malan Ice Caps contain 59 glaciers with a total area of 189.7 km^2. The largest glacier (Glacier No.14) is located on the southern slope, with an area of 30.4 km^2.

The XM is weakly affected by the westerly circulation and monsoon circulation. The mean annual air temperature is approximately −10 ℃ and the annual precipitation is 173−494 mm in Hoh Xil (Li, 1996). More than 90% of the precipitation is concentrated between May and September, therefore, the glaciers in this region belong to the summer-accumulation type (Li, 1996). Xie et al. (2000) reported the annual precipitation of the Taiyanghu basin on the side of the Malan Ice Caps was 170 mm, with approximately 80% of the precipitation concentrated during the warm season (from May to October). And near the snowline of Xinqingfeng, the average elevation was 5440 m, the annual average air temperature

was −15.4 ℃, and the annual precipitation was 340 mm (Xie et al., 2000). The average elevation of the snowline at the Malan Ice Caps was 5445 m and the air temperature was estimated as −11.5 ℃ (Xie et al., 2000). Based on a 107.07 m ice core recorded from the Malan Ice Cap in May 1999, there has been a warming trend during the 20th century and the warmest period recorded was during the 1950s to the early 1980s. There have also been several colder stable periods during the warming period, with a colder climate during the late 1980s to 1990s (Wang et al., 2003).

3 Data and methods

3.1 Topographic maps

Four topographic maps with a 1:100,000 scale (sheet numbers: I-46-2, I-46-3, J-46-134 and J-46-135) were constructed from aerial photographs taken between 1970 and 1971 by the State Bureau of Surveying and Mapping of China (SBSMC) and used in glacier outlines digitised for the first CGI. The contour lines of three of the topographic maps, except for J-46-134, were obtained from the SBSMC and were georeferenced to the WGS84/EGM96 using a seven-parameter transformation method. These were then interpolated into DEMs (hereafter, referred to as TOPO DEMs) with a spatial resolution of 30 m. These TOPO DEMs covered the entire Malan area and a small portion of Xinqingfeng. The contour lines of the topographic maps were derived manually using an analytical plotter, and the accuracy of these was strictly controlled and verified based on the photogrammetric Chinese National Standard (GB/T12343.1-2008, 2008). The plane root mean square error (RMSE) for topographic maps with a 1:100,000 scale was less than 0.5 mm for flat and hilly areas (with slopes of $< 2°$ and 2–6, respectively) and less than 0.75 mm for the mountain areas and high mountain areas (with slopes of 6–25 ° and $> 25°$, respectively). The vertical RMSE of these topographic maps were less than 6–10 m for flat and hilly areas and less than 16–28 m for the mountain areas and high mountain areas. Because the slopes of most of the glacierised areas in the study area were gentle (~12 °), the plane and vertical accuracy of the TOPO DEMs were better than 0.75 mm and 16 m on glaciers, respectively. The digital contour lines were from SBSMC, which were produced and inspected in strict accordance with the photogrammetric Chinese National Standard (GB/T12343.1-2008, 2008). We converted these lines to Grid DEM using the triangular irregular network (TIN) method, which produces a higher accuacy while meeting the Chinese National Standard (GB/T12343.1-2008, 2008) and reflects the true mountainous terrian much better (Wang et al., 2014). Table 1 shows that TOPO DEMs were acquired during the winter season (between October and December). To accurately estimate the glacier mass balance, the possible seasonal mass changes during winter need to be corrected. However, both snowfall and melt mainly occur during summer (June to September), i.e. glaciers in XM are summer-accumulation type glaciers (Wang et al., 2003; Xie et al., 2000) and no obvious glacier mass change occurs during the winter months (Liu et al., 2019). Consequently, we assumed that no seasonal variation occurred between October and December in our study.

3.2 ASTER

The ASTER sensor onboard the TERRA satellite platform provides a stereo pair generated by nadir-looking (3N, 0.76–0.86 μm) and backwards-looking (3B, 27.7 ° off-nadir) cameras with a base-to-height ratio of approximately 0.6. This value is close to ideal for generating DEMs with a variety of terrain conditions via automated techniques (Kamp et al., 2003). We used the AST14DMO products available at the EARTHDATA website (https://search.earthdata.nasa.gov/search, Table S1). This product has been derived from the raw ASTER data by the Land Processes Distributed Active Archive Centre using orbital ancillary data, without ground control points (GCPs). ASTER DEMs for 2014 and 2018 were also used in surging glacier analysis.

3.3 TerraSAR-X/TanDEM-X

The TerraSAR-X was launched in June 2007 followed by its twin satellite, the TanDEM-X, in June 2010. The two satellites fly in a close orbital formation and act as a flexible baseline configuration (Krieger et al., 2007). Five pairs of TerraSAR-X/TanDEM-X (TSX/TDX) data in the experimental co-registered single look slant range complex (CoSSC) format acquired in the bistatic InSAR stripmap mode were employed in our study (Table 1). The CoSSC product was focused and co-registered at the TanDEM-X Processing and Archiving Facility using an integrated TanDEM processor. GAMMA SAR and interferometric processing software were used to process the CoSS product (Neckel et al., 2013). There are two methods for calculating the elevation change when employing TSX/TDX and SRTM DEM. The first method is differential interferometric SAR (D-InSAR) and the second method is DEM differencing. For the bistatic mode, neither the deformation nor the atmospheric delay phase was included in the interferogram and the phase resulting from noise was also ignored.

The SRTM 1 and TSX/TDX were co-registered before constructing the differential interferogram. This required establishing an initial look-up table based on the relationship between the map coordinates of the SRTM 1 DEM and the SAR geometry of the TSX/TDX master file. The offsets between the master image and the simulated intensity image of the SRTM 1 DEM used an optimisation of the simulated SAR images by employing GAMMA's *offset_pwrm* module. The SRTM 1 DEM was then transformed into a SAR geometry for the TSX/TDX master image. The simulated interferometric phase ($\Delta\emptyset_{\mathrm{TSX/TDX}}$) from the SRTM 1 DEM ($\Delta\emptyset_{\mathrm{SRTM}}$) was subtracted from the interferometric phase of the TSX/TDX data. The D-InSAR phase ($\Delta\emptyset'_{\mathrm{diff}}$) can be obtained from Eq. (1):

$$\Delta\emptyset'_{diff} = \Delta\emptyset_{TSX/TDX} - \Delta\emptyset_{SRTM}\ , \quad (1)$$

The differential interferogram was filtered using an adaptive filtering approach. The flattened differential interferogram was unwrapped using the minimum cost flow algorithm (Costantini, 1998). The areas of layover and shadow with low coherence (< 0.3) were masked out during the unwrapping processing. The unwrapped differential phases were converted to absolute differential heights using the calculated phase-to-height sensitivity. The differential interference uncertainty caused by baseline errors was regarded as a systematic error. A two-dimensional first-order polynomial fit for the non-glacial regions

was used to remove the residuals in the glacial regions. Finally, a map with a spatial resolution of 12 m from the SAR coordinates was geocoded to the geographic coordinates using a refined look-up table. During the above process, the elevation difference between SRTM and TSX/TDX was derived directly from D-InSAR. The TSX/TDX DEM was geocoded to the geographic coordinates with a grid posting of one arc second using the refined geocoding lookup table created above, and TSX/TDX DEM was produced. We calculted the DEM difference using this DEM that was compared to TOPO.

3.4 SRTM and radar penetration

The SRTM DEM was acquired from interferometry of C-band and X-band radar from 11 to 22 February 2000. These data are representative of the glacier surface at the end of the 1999 ablation period with slight seasonal variances (Gardelle et al., 2013). The 1″ C band DEM (SRTM 1) and the 3″ C-band DEM (SRTM 3) are freely available and cover most of the globe. The accuracy of the SRTM is specified as 16 m with a 90% confidence level and varies according to the region (Berthier et al., 2006). The X-band SAR system has a narrower swath width than that of the C-band SAR and, unfortunately, we could not access any X-band SRTM DEM data in our study area. Therefore, we used the SRTM C-band DEM at EGM96 orthometric heights with a 30 m pixel resolution (SRTM 1) in our study. When the SRTM C-band DEM was used in D-InSAR or DEM differencing with TerraSAR-X/TanDEM-X, which has an X-band SAR system, the results were directly corrected by the difference between the SRTM C-band and X band DEM, assuming that no seasonal variation occurred between February and April when there was little snowfall and no obvious melt (Xie et al., 2000).

The penetration of the C-band radar into snow and ice must be considered when assessing changes in the glacier elevation determined by the difference between the SRTM C-band DEM and TOPO DEM (Gardelle et al., 2012a). It is difficult to estimate exactly the penetration depth of the C-band radar into snow and ice for XM glaciers. There are three methods for evaluating the C-band radar penetration. The first method is by comparison between the SRTM C-band and X-band assuming that the penetration depth of the X-band is negligible (cf. Gardelle et al., 2012a). Several studies have reported a penetration depth of 2.1–4.7 m for a radar beam at ~10 GHz targeting an Antarctic ice sheet and showed that the penetration depth varies with the water content of the surface snow cover (Davis and Poznyak, 1993; Surdyk, 2002). Glaciers in our study area have higher temperatures and more snow moisture than those of the Antarctic ice sheet. Besides, the glacier surface elevation of SRTM-C acquired in mid-February 2000 roughly refers to the state of glaciers at the end of the ablation period for 1999 in our study. We assumed that the slight penetration of SRTM-X into the snow and ice was offset by the slight seasonal change caused by the time interval (from the end of the ablation period for 1999 to mid- February 2000). Consequently, this method was appropriate for our study because of the assumption that the effect of the slight penetration of the X-band is negligible compared to other confounding factors. The second method follows the methodology decribed by Wang and Käab (2015). We linearly extrapolated the time series of the elevation from ASTER DEMs (AST14DMO

products, Table S1), which was corrected by three-dimensional (3-D) coregistration (Nuth and Kääb, 2011) using SRTM DEM as the reference DEM off-glacier, to reconstruct the glacier topography in mid-February 2000. Then, the penetration depth of the C-band radar signal over XM glaciers was generated by subtracting the SRTM DEM from this reconstructed DEM (Berthier et al., 2016). The third method is the comparison between ICESat GLA 14 footprints from 2003 to 2004 and SRTM DEM as described by Kääb et al. (2012). We used the elevation change rate between the footprints acquired in 2003 and 2004 to linearly extrapolate to mid-February 2000. These three methods have their respective advantages and disadvantages. Among them, the first one ignores the X-band radar penetration, and the second one does not have good performance in accumulated areas such as glaciers owing to image matching failure when clouds, shadow, and fresh snow coverage are present, and the third one has a very large uncertainty because of the large footprint sizes and insufficient spatial sampling of the ICESat measurements. We compared these results with Zhou et al. (2019) and found that these results had little difference, especially that the result of the first method was close to the third and Zhou et al.'s (Table 2). The result of the second method was slightly larger than that of the first, which might be owing to the X band radar penetration. In our study, the SRTM elevation roughly referred to the state of glaciers at the end of the ablation period for 1999, and thus the slight X-band radar penetration could be offset by the slight seasonal change. There are too many data voids (~40%) in the results of the second method and the insufficient spatial sampling of the ICESat measurements in the third method. Thus, we used the first method to estimate the C-band radar penetration. Thus, we used the first method to estimate the C-band penetration by comparing the SRTM-C band with the SRTM-X band DEM (cf. Gardelle et al., 2012a) in two regions near our study region (northeast by 45 km and southeast by 25 km) where the glaciers are at an elevation of 4930–5950 m a.s.l. Nearly 92% of the glacial region in the XM is in this elevation range. We also estimated the penetration for higher than 5950 m a.s.l. or lower than 4950 m a.s.l. using the observed value for 5950 m a.s.l. and 4950 m a.s.l. (Fig. 2).

3.5 Glacier velocity data

To investigate the dynamic behaviour of the surging glacier, we used the glacier velocity acquired from the Inter-Mission Time Series of Land Ice Velocity and Elevation (ITS_LIVE) and the Global Land Ice Velocity Extraction from Landsat 8 (GoLIVE) dataset. In addition, we supplemented some data from 2008 to 2009 using ENVI add-on COSI-Corr derived from Landsat TM images. Landsat level 1T data were assumed to be quasi-coregistered due to the same sets of GCPs and vertical references used for orthorectification (Shangguan et al., 2015). We selected a signal-to-noise ratio > 0.9 to filter obvious outliers and errors caused by clouds, and topography, and low image contrast was removed from the matching result.

The ITS_LIVE data product is a set of regional compilations of annual mean surface velocities for major glacier-covered regions, spanning the period from 1985 to 2018, and is subject to image availability and quality. Surface velocities were derived from Landsat 4, 5, 7, and 8 imagery using the auto-RIFT feature tacking processing chain described in Gardner et al.

(2018). Data scarcity and/or low radiometric quality were significant limiting factors for many regions in the earlier product years. Annual coverage is nearly complete for the years following the Landsat 8 launch in 2013.

GoLIVE is a compilation of ice velocities derived from the cross-correlation of pixel positions in pairs of panchromatic Landsat 8 images acquired from May 2013 to the present (Fahnestock et al., 2016). We considered only the velocities of the peak correlation values (corr) >0.4 and the differences in correlation values between the primary and secondary peaks (del_corr) <0.3 (Sam et al., 2018). We calculated the mean or maximum velocities for all velocity rasters over each of the different years. We then discarded any annual average velocity pixels that were over 1 standard deviation from the mean velocity values.

3.6 Glacier boundary mapping, and the calculation of the area change and uncertainty

The glacier boundaries of 1970/71 were derived from the first CGI, which was inventoried using topographic maps and verified using aerial and Landsat MSS images. The glacier boundaries of 2000, 2013 and 2018 were digitised manually from Landsat images using the same method as that for the second CGI processing (Guo et al., 2015). We also checked the glacier boundaries by cross-checking with Google Earth imagery.

The uncertainty in determining glacier boundaries (E_a) was estimated using a buffer of 13.5 m for the topographic maps with a 1:100,000 scale and half a pixel for the Landsat images (Wei et al., 2014). The uncertainty of the glacier area change (E_{ac}) was calculated using Eq. (2):

$$E_{ac} = \sqrt{{E_{a1}}^2 + {E_{a2}}^2}\,, \tag{2}$$

where E_{a1} and E_{a2} represent the uncertainties of the glacier areas for the two different periods.

3.7 Glacier length

In the present study, we estimated the glacier lengths by generating glacier centrelines using an automated method. This approach was based on the glacier axis as derived from the glacier morphology, which requires glacier outlines and DEMs as the inputs (Yao et al., 2015). The glacier centreline was derived from the SRTM DEM and glacier outline with the largest area. We split the glacier centreline with the glacier outlines in the different periods and calculated the associated glacier lengths.

Similar to the uncertainty of glacier boundaries, the uncertainty of glacier lengths was also estimated using a buffer of 13.5 m for the topographic maps with a 1:100,000 scale and half a pixel for the Landsat images. The final uncertainty was also calculated using Eq. (2), where E_{ac} represents the uncertainty in the changes of the glacier lengths and E_{a1} and E_{a2} represent the uncertainties of the glacier lengths from two different times.

3.8 Glacier elevation changes, mass balance and uncertainty

Changes in glacier elevation from 1999 to 2011/12 were calculated using the D-InSAR based on the TSX/TDX and SRTM C-band (see Section 3.3). Changes in the glacier elevation from 1970/71 to 1999 and from 1970/71 to 2011/12 were calculated by taking the differences between the DEMs for the TOPO DEM, SRTM and TSX/TDX DEM. All DEMs were resampled to the same spatial resolution (30 m). Before the DEM differencing, the DEMs were corrected for planimetric and altimetric shifts (Nuth and Käab, 2011) using the TOPO DEM as a reference. Then, the curvature bias (Gardelle et al., 2012a) in the glacial region was corrected by fitting sixth-order polynomials to the elevation differences for the non-glacial regions. We considered only the elevation differences between ±100 m over the stable region with slopes ranging from 5 ° to 75 ° and excluding glaciers and water bodies in the co-registered and bias corrected DEMs. After the adjustments (Fig. S1), an elevation difference map of off-glaciers indicated a local random noise; however, at length scales of a few kilometres, the elevation differences were small, with the mean elevation difference of the total region less than 0.5 m (Table 3).

The geodetic mass balance (m w.e. a^{-1}) was calculated using the following equation (Fischer et al., 2015):

$$\dot{B} = \frac{\overline{\Delta z} \cdot A_l \cdot f_m}{\bar{A} \cdot \Delta t} \ , \quad (3)$$

where $\overline{\Delta z}$ is the average elevation differences within the perimeter covered by an individual glacier in a larger extent of two periods. In this case, the larger glacier extent ensured the mass change results were not affected by glaciers advancing or retreating. A_l is the glacier area when covered in a larger extent. $\bar{A}$ is the average area between two periods calculated as $(A_{t1} + A_{t2})/2$ and Δt is the length of the observation period (t_2 - t_1) in years, f_m is a conversion factor (without units) used to transform glacier elevation change into mass change and is set as a constant of 0.85 corresponding to a density of volume change of 850 ±60 kg m^{-3} as a reasonable and widely used assumption over longer periods (Huss, 2013).

Under ideal circumstances, there would be no elevation difference in the stable region after the above adjustments. However, the residual errors (Fig. S1-S6 and Table 3) still existed in our results and caused uncertainty for the elevation change of the glacial region. Therefore, the uncertainty in the differences of the glacier elevation ($E_{\Delta H}$) was estimated using the mean elevation difference (E_{med}) and standard deviation (σ) of the off-glacier region. We calculated the differences of the glacier elevation for each altitude band (50 m, $E_{\Delta Hi}$), which excluded glaciers and water bodies:

$$E_{\boldsymbol{\Delta Hi}} = \sqrt{{E_{medi}}^2 + {\sigma_i}^2 / N_{effi}} \ , \quad (4)$$

$$N_{effi} = N_{toti} \cdot PS/2d \ , \quad (5)$$

where E_{medi} and σ_i are the mean elevation difference and the standard deviation for each altitude band, respectively. N_{effi} is the effective number of observations at off-glacier region, i.e. the number of included pixels, and is calculated using the total number of observations (N_{toti}) for each altitude band, the pixel size and d, the distance for the spatial autocorrelation of the elevation change maps (1410 m) was determined using Moran's I autocorrelation index for the elevation differences of off-

glacier region (Bolch et al., 2011; Gardelle et al., 2013). The overall uncertainty of the DEM difference was calculated by the glacier area weighted average of $E_{\Delta Hi}$ for each altitude band.

The uncertainty of the glacier boundaries (E_a) should be considered in the mass balance estimation. The glacier outlines were used as they have a larger extent during the investigated period. The uncertainty in radar penetration (E_p) should also be considered during the mass balance estimation. However, it is difficult to understand this uncertainty. We used the uncertainty in the DEM difference between the SRTM-X and SRTM-C using Formula (4) to represent E_p and the results revealed an uncertainty of 1.9 m. The radar penetration accuracy includes the uncertainty of the differences between SRTM-X and C and the possible slight penetration of the X-band radar beam. However, it was impossible to evaluate the radar penetration accuracy. It was assumed that the possible slight penetration of the X-band radar beam was within this uncertainty range. Finally, the uncertainty of the volume to mass conversion should also be considered to calculate the final uncertainty (*Em* of ±60 kg m^{-3} for the elevation change to mass change) (Huss, 2013):

$$E = \sqrt{E_{\Delta H}{}^2 + (\frac{\Delta H \cdot E_a}{S})^2 + E_p{}^2 + (\frac{\Delta H \cdot E_m}{\rho})^2}\ , \quad (6)$$

where S represents the glacier area and ρ represents the ice density.

4 Results

4.1 Glacier area and length changes

There were 136 glaciers in XM with a total area of 641.2 ±7.7 km^2 in 1970/71. Nearly 89% of the glacier areas were between 5100–5900 m a.s.l. (Fig. 3). The maximum elevation of the glaciers at Xinqingfeng (6,821 m a.s.l.) was higher than that at Malan (6013 m a.s.l.), and the mean median elevation (5,552 m a.s.l. in 1970/71, 5,560 m a.s.l. in 2018) was also higher than in Malan (5,525 m a.s.l. in 1970/71, and 5,533 m a.s.l. in 2018).

The total glacier area insignificantly decreased by 27.4 ±8.9 km^2 (4.3 ± 1.4%) or 0.09 ±0.03% a^{-1} from 1970/71 to 2018. The glacier area only decreased by 0.01 ± 0.20% a^{-1} from 2013 to 2018, but it decreased by 0.03 ± 0.12% a^{-1} and 0.13 ± 0.06% a^{-1} for the periods from 2000 to 2013 and 1970/71 to 2000, respectively. The glacier area at Xinqingfeng decreased by 0.08 ±0.03% a^{-1}, while at Malan it decreased by 0.11 ± 0.03% a^{-1}. The glaciers showed heterogeneous variations with some advancing or surging (Tables 4 and 5). Overall, the shrinkage speed of the glacier area decreased after 2000 and the glacier area was stable after 2013, which can be mainly attributed to the heterogeneous variations with some of the glaciers advancing or surging (Tables 4 and 5).

4.2 Glacier mass changes

The average elevation decrease of glaciers in Xinqingfeng was 3.50 ± 2.17 m, resulting in an average glacier mass loss of 0.22 ± 0.17 m w.e. a^{-1} between 1999 and 2011/12. Glaciers exhibited heterogeneous mass changes. West Monuomaha

Glacier experienced a significant lowering on the tongue, resulting in a net mass loss from 1999 to 2011 (Fig. 4). Glacier Nos. 5–7 had mass gains of 0.01 ± 0.16 to 0.10 ± 0.16 w.e. a^{-1} (Fig. 4 and Table 6).

The glaciers at Malan decreased in elevation from 1970 to 2012 with an average of thinning of 10.72 ± 0.91 m, resulting in an average mass loss of 0.22 ± 0.02 m w.e. a^{-1}. The rate of mass loss for these glaciers increased from –0.19 ±0.14 m w.e. a^{-1} between 1970 and 1999 to -0.29 ±0.17 m w.e. a^{-1} between 1999 and 2012. Glacier Nos.14 and 15 experienced a slightly positive mass budget from 1970 to 1999.

Our results (Fig. 5) indicate that ice loss mainly occurred below 5600 m a.s.l., which is the reason for glacier area loss below 5600 m a.s.l.. The ice thickness thinning rate below 5600 m a.s.l. between 1999 and 2012 was higher than that between 1970 and 1999. However, ice thickness thickened obviously below 5000 m a.s.l. during 1999-2012, which was caused by some glacier surging.

4.3 Glacier advance and surge

A minimum of seven glaciers at Xinqingfeng and Malan showed heterogeneous variations with either surging or advancing during different periods (Table 7). The eastern branch of Glacier No. 1 advanced 280 ± 20 m and converged into the West Monuomaha Glacier (No.2) from 1971 to 1987 at the same time that the West Monuomaha Glacier was retreating. Glacier No. 1 then continued to advance 50 ± 20 m from 1989 to 1999. The average advance rate for the West Monuomaha Glacier during 1987–1998 was 130 ± 10 m a^{-1}, where the peak value was 600 ± 10 m a^{-1} during 1987–1989. The West Monuomaha Glacier had a higher velocity during 1986–1997 with a maximum velocity of 150 m a^{-1} based on the time series data for glacier velocities derived from ITS_LIVE (Fig. 6a). However, some data was mising between 1987 and 1989. According to advancing magnitude (1200 m) during 1987–1989, we assumed that the West Monuomaha Glacier had a much higher velocity with surging during 1987–1989. We found this glacier had a higher velocity from 12 October, 1987 to 29 Novermber, 1987 with a maximum velocity of 5.6 m d^{-1} (Fig. 6b), which may be the peak value from 1986 to 2001. Consequently, the West Monuomaha Glacier was a surging glacier with a higher velocity from 1986 (or before 1986) to 2001.

The Monuomaha Glacier (No.4) also advanced 1160 ± 20 m from 2010-2016; however, it had an overall retreat of 2550 ± 20 m over the entire period from 1970 to 2010. The glacier velocity results (Figs. 7a and 7b) suggest that the Monuomaha Glacier could have been initiated at some point between February and March, 2009. The velocity of Monuomaha Glacier fell abruptly in January 2017 and then returned to normal levels by 2018 based on the time series data for glacier velocities derived from GoLIVE and ITS_LIVE. The Monuomaha Glacier experienced a significant thickening in the lower part and a significant lowering in the higher part during 1999-2011 and 2011-2014 (the difference between ASTER and TSX/TDX-X, Fig. 7c), which is the signal for surging. The Monuomaha Glacier showed terminus thickening between 2014 and 2018 (the

difference between ASTER DEMs), and there were some unreasonable data on the accumulation zone due to higher uncertainty with DEMs derived from optical images for the fresh snow cover region.

The Zu Glacier (No.6) advanced 50 ± 10 m from 2014 to 2016 and also experienced a higher velocity from 2013 to 2015 (Fig. 8). The Zu Glacier showed a significant thickening in the lower part and a significant lowering in the higher part during 2014–2018 (Fig. 8c). Combined with the shape of the terminus of the Zu Glacier (Fig. 8d), this glacier might be surging from 2014 to 2016, with this glacier retaining a relatively high speed until now.

Glacier No. 7 advanced 40 ± 20 m from 1986 to 1989, and then suddenly advanced by 110 ± 20 m from 2009 to 2010. Glacier No. 8 advanced 430 ± 20 m from 1970 to 2000; however, we only know for certain that this glacier advanced 660 ± 20 m from 1970 to 1986 and then retreated between 1986 and 2018. Glacier No. 14 showed significant thickening and thinning within its tongues (Fig. 4b) between 1999 and 2012. We found that Glacier No. 14 advanced 260 ± 20 m from 2007 to 2012, however, it retreated 950 ± 20 m between 1971 and 2007. Thus, Glacier No. 14 might be a surging glacier.

The latest surge-type index from Mukherjee et al. (2018) classified the West Monuomaha Glacier, Monuomaha Glacier, and Glacier No.7 as surge-type glaciers (>100 m a^{-1}). Our results showed that the Monuomaha Glacier and Glacier Nos. 7, 8, and 14 showed significant thickening in their tongues and a significant lowering in their upper parts (Fig. 4b), and these glaciers might be surging glaciers. While Glacier No. 8 was considered a surge-type glacier with surging from 1999 to 2011, it is unclear whether its advance from 1970 to 1986 was caused by surging. In addition, we also found that Glacier No. 1 was likely a surge-type glacier (<100 m a^{-1} and >10 m a^{-1}) (Mukherjee et al., 2018).

5 Discussion

5.1 Uncertainties

The uncertainties in the geodetic mass balance mainly resulted from the precision of the DEM acquisitions and processes, glacier boundaries and changes, seasonal variation, radar penetration depth and data voids. All DEMs and methods for acquisitions and processing we employed proved to be valuable for assessing geodetic glacier mass budgets and evaluating uncertainties in our study. Even if TOPO DEMs were produced and inspected in strict accordance with the photogrammetric Chinese National Standard (GB/T12343.1-2008, 2008), we assumed that low contrast surfaces affected the elevation in case of snow cover. Thus, we divided each glacier into an accumulation region and ablation region by mean median elevation. And we set the elevation of the accumulation regions to zero assuming only minor elevation changes for these areas. Then the difference between the results for mass change using this method and our results were less than 0.05 m w.e. a^{-1}. This number was included in the uncertainty terms.

The uncertainty resulting from glacier boundaries was also evaluated in our study. However, the smallest glacier size inventoried in our study was 0.01 km^2, which could create a 10% error in the estimation of the ice volume (Bahr and Radić,

2012). It was difficult to assess this error due to little knowledge of the amount, area, and specific mass balances of the smallest glaciers (including glaciers with area < 0.01 km^2). Thus, we conservatively assumed that the underestimation made a 10% error in the loss of ice volume. Consequently, an error of approximately 0.02 m w.e. a^{-1} was caused by the smallest glaciers. This number was also included in the uncertainty terms.

Seasonal variance caused by the difference between data acquisition times should be considered because geodetic measurements should show the mass balance corresponding to an integer number of balance years. For XM glaciers, most accumulating and melting occurred simultaneously during the summer (June to September). In addition, based on the extent of snow coverage on XM glacires from the Landsat images, we assumed that September was the end of the ablation period. Therefore, in our study, the correction of seasonal variation was set to zero, because no obvious glacier mass change occured between the months of late winter and spring. Even so, we still conservatively assumed that the seasonal mass change was equal to the maximum net accumulation (603 mm w.e.) of the Malan ice core over the period from 1887 to 1998 (In fact, the average net accumulation of the Malan ice core over the period from 1887 to 1998 was only 186 mm w.e.). This value could create errors between 0.01 and 0.05 m w.e.a^{-1} for the mass balances for the periods of 1970–1999, 1999–2012, and 1970–2012. The number was also included in the uncertainty terms.

One critical issue in our study was the unknown C-band and X-band radar penetration into snow and ice. We estimated the C-band radar penetration by comparing the SRTM C-band with the X-band DEM without considered X-band radar penetration. Because TSX/TDX and SRTM-X have the same band (X-band), and the seasonal variation could be ignored as above, it was unnecessary to consider additional X-band penetration when calculating the elevation change between TSX/TDX DEM and SRTM-C DEM, even if the penetration depth of the X-band radar signal into the glacier surface was influenced by different seasons. Liu et al. (2019) found that the X-band penetration in January was 0.61 $\pm$0.06 m higher than that in April over the Puruogangri ice field. We also assumed that the X-band penetration in February was 0.61 $\pm$ 0.06 m higher than that in March and April over the XM glaciers, potentially creating errors of up to 0.04 m w.e.a^{-1} for the mass balances during 1999–2012. However, since additional X-band radar penetration was not considered, the penetration depth of the C-band radar we obtained was likely underestimated when calculating the elevation difference between TOPO DEM or TSX/TDX DEM and SRTM C-band DEM. Several studies have reported that the average penetration depth of the X-band radar could reach 2–4 m or less under dry-snow conditions over the accumulation region of glaciers in the Karakoram (Round et al., 2017) and Western Pamir (Lambrecht et al., 2018). However, the precipitation in this region is much less than that in the Karakoram and Western Pamir, especially during winter, and the thickness and extent of the dry snow might be much less than that in the Karakoram and Western Pamir. We conservatively assumed that the X-band radar depentration was 2 m, with the updated results only less negative by 0.06 m w.e. a^{-1} and 0.04 m w.e.a^{-1} than our results during 1970–1999

and 1970–2012, respectively. The number was also included in the uncertainty terms. Thus, the geodetic mass balance results over the long term were less affected by X-band penetration.

Another major uncertainty for the geodetic mass balance was caused by the lack of information in several data voids. Our elevation difference results did not exceed the range of ±100; therefore, there were no data voids in the difference between TOPO and SRTM. The elevation difference in the areas of layover and shadow with low coherence (<0.3) for TSX/TDX was not accurate and was excluded in our study. Then, there were only a small data voids (approximately 1%) for the elevation difference between TOPO or SRTM and TSX/TDX. In the present study, we calculated the mean elevation difference of the nonvoid pixels without considering the data voids. Some methods can be used to fill the data voids. McNabb et al. (2019) split these methods into three general categories: constant interpolation, spatial interpolation, and hypsometric interpolation. In constant methods, the maximum, minimum, mean and median elevation changes observed in the same elevation bins regions are used to fill the voids and to evaluate the impact on the total glacier mass balance. In spatial interpolation, the raw DEM or elevation differences of the surrounding pixels are interpolated to fill the voids, and the average elevation difference according to the on-glacier pixels within a 1 km radius of the void pixel for each void pixel is calculated. In hypsometric methods, the mean elevation difference for each 50 m wide elevation bin is used to calculate the mass change by the glacier area of each elevation bin. The above different assumptions led to a variation of the mass balance of less than 0.04 m w.e. a^{-1}. The number was also included in the uncertainty terms.

5.2 Glacier area changes

Our results showed a decrease in the glacier area at a rate of ~0.00–0.26% a^{-1} (except for Glacier Nos. 1, 2, and 8) from 1971 to 2018. These results are in agreement with other studies, proving that there are low rates of glacier shrinkage in the ITP. For example, there was an 0.18% a^{-1} shrinkage from the 1970s to 2009 for the drainage Basins of Ayakkum Lake (5Z11, basin code from CGI) and Hoh Xil Lake (5Z12), 0.17% a^{-1} from 1976 to 2013 for the Qaidam interior-drainage basin (5Y5), and 0.14 % a^{-1} from 1976 to 2013 for the Ayakkum Lake interior-drainage basin (5Z1) (Wei et al., 2014; Ye et al., 2017).

Compared with the surrounding regions in the ITP, the rate of glacier shrinkage in the XM was very close to the western Kunlun Shan (0.1% a^{-1} from 1970-2010) (Bao et al., 2015) and Kangzhag Ri (0.08% a^{-1} from 1970 to 2016) (Zhang and Liu, 2018), was slightly lower than Geladandong (0.15% a^{-1} from 1964 to 2010) (Wang et al., 2013) to the south, and was significantly lower than Dongkemadi (0.26% a^{-1} from 2000-2011) (Qiao, 2010) and Qilian Shan (0.39% a^{-1} from 1956 to 2010) (Sun et al., 2018) to the northeast, Bugyai Kangri (0.48% a^{-1} from 1981 to 2013) (Liu et al., 2015) to the southeast, and western Nyainqentanglha (0.62% a^{-1} from 1970 to 2014) (Wu et al., 2016) to the south.

5.3 Glacier mass changes

Our results for the mass changes of the glaciers at Xinqingfeng and Malan of −0.22 ± 0.17 m w.e. a^{-1} and −0.29 ± 0.17 m w.e. a^{-1}, respectively, from 1999 to 2011 agree well with the results from Zhou et al. (2019) of −0.21 ± 0.10 m w.e. a^{-1} and −0.22 ± 0.10 m w.e. a^{-1} from 2000 to 2016. Brun et al. (2017) reported that the global average mass loss was 0.14 ± 0.07 m w.e. a^{-1} from 2000 to 2016 for glaciers in the ITP. We also estimated that there was a mass loss of 0.17 m w.e. a^{-1} for the glaciers at XM based on the data from Brun et al. (2017) (Table 6), which agrees well with our study. However, Gardner et al. (2013) found a −0.01 ± 0.35 m a^{-1} elevation change for the glaciers of the ITP from 2003 to 2009 using ICESat and SRTM. This deviation may be attributed to the different study periods and extent. Neckel et al. (2014) determined that the average mass loss was 0.77 ± 0.35 m w.e. a^{-1} from 2003 to 2009 for the glaciers in the Qilian Mountains and East Kunlun, which were included in our study region, as observed by ICESat GLAS. Their estimated trend was significantly more negative than ours, which may be attributed to a different study extent and period. These results together prove that the very large ITP is an aggregation of climatically heterogeneous sub-regions that result in spatial variability in the glacier mass balance. Previous studies (Bao et al., 2015; Lin et al., 2017) have reported that the West Kunlun Shan and extended West Kunlun showed glacier mass gain from 2000. Zhang and Liu (2018) determined that glaciers in Kangzhag Ri, which are approximately 70 km west of XM, showed a positive mass balance (+ 0.16 ± 0.02 m w.e. a^{-1}) from 1999 to 2012 using ASTER and SRTM. Therefore, KangzhagRi and XM are the transition zones from the west to the east regarding the mass balance distribution from positive to negative based on the data since 1999. In addition, we compared three glacial clusters along approximately 35.5–36.5 °N, from 87 °E to 91 °E (Ulugh Muztagh, Kangzhag Ri, and XM) using the results from Brun et al. (2017), which showed that the mass balance decreased from the west to east (Fig. 8a). We also calculated the mean median elevation, which was presumed to be at equilibrium-line altitude (ELA) such that the mass balance is zero at that elevation (Sakai et al., 2015), for three glacial regions (Fig. 8c) and showed the mean median elevation (or ELA) also showed a decrease from the west to the east. The other three glacial clusters (Zangsar Kangri, Purogangri, and Geladandong) along approximately 33–34.5 °N, from 85.3 °E to 91.5 °E also showed a similar trend (Figs. 8b and d). Because the mean median elevation (or ELA) is closely related to air temperature and precipitation (Sakai et al., 2015), different climate zones result in heterogeneity with the glacier mass balance. In XM, a local climatic zone, the area average mass balance was calculated with a mean median elevation interval of 50 m using our results from 1999 to 2012 (Fig. 9). The results showed that the glacier mass loss decreased with increasing mean median elevation. Glaciers with a mean median elevation below 5700 m a.s.l. had significantly more negative mass balance than glaciers above 5700 m a.s.l., because ice mass loss mainly occurred at low altitudes (Fig. 5). However, there were no obvious relationships between mass balance with mean median elevation for glaciers with a mean median elevation below 5700 m a.s.l. Thus, glaciers at XM were also significantly influenced by local heterogeneity of climate.

Most glaciers experienced similar mass budgets for the investigated periods at Malan. However, some glaciers had greater negative budgets after 1999, e.g. Malan experienced a slight mass gain before 1999 and a negative mass change after 1999. The global average mass change trend (more negative) was in agreement with Bugyai Kangri, Dongkemadi and West Geladandong to the southeast of XM (Chen et al., 2017). However, this was in contrast to KangzhagRi (Zhang and Liu, 2018) and Aru Co to (Zhang et al., 2018) to the west of XM, which showed more positive growth after a negative period. Glaciers to the west of XM showed a lower mass loss or a mass gain trend after 1999, however, glaciers to the east showed a more negative change.

5.4 Glacier advance and surge

Two surge models have been linked to a corresponding hypothesis relative to thermal or hydrological surge control (Falaschi et al., 2018; Quincey et al., 2015). Thermal control is characterised by an initiation phase that lasts several years before reaching a peak in the surge and a termination phase that consists of several years of deceleration following the surge peak (Clarke et al., 1984; Murray et al., 2000). A switch in basal thermal conditions has been identified as a surge mechanism for some polythermal glaciers, with surging occurring when cold basal conditions switch to temperate conditions (Clarke et al., 1984; Fowler et al., 2001; Murray et al., 2000). These surges can begin or end at any seasonal time of year. Hydrological control can explain surging for temperate glaciers and many polythermal glaciers that are already temperate at the base (Sevestre et al., 2015). The subglacial drainage system becomes inefficient during the winter months, increasing the subglacial water pressure and facilitating rapid sliding (Björnsson, 1998; Kamb et al., 1985). This is characterised by the rapid acceleration and deceleration over a short time (i.e., days to weeks) and is initiated during the winter months and terminated during the summer months when the subglacial drainage system becomes highly efficient (Burgess et al., 2012; Lingle and Fatland, 2003). The borehole temperature measurement results in the Malan Ice Caps showed that the ice temperature at a depth of 10 m was −6.5℃, therefore, the glaciers in our study were attributed to the cold type. Our results showed that the Monuomaha Glacier had a long duration active phase that lasted 8 years and may have begun and ended in the winter. Thus, the Monuomaha Glacier might be surge controlled via thermal mechanisms, where a switch from cold to temperate conditions caused the surge onset in 2009. The West Monuomaha Glacier and Zu Glacier also had a long duration for the active phase and might be the same surge control as the Monuomaha Glacier. Under the colder and wetter climate that was recorded in the ice core of Malan ice cap from the late 1980s and into the 1990s (Wang, 2009; Wang et al., 2003), more snowfall may have occurred in the XM. In recent years, higher precipitation including snowfall has occurred in the XM (Fig. 10). Moreover, the Zu Glacier exhibited a positive mass balance (0.07 ± 0.16 m w.e. a^{-1}), which might be attributed to the precipitation (snowfall) increases from 1999 to 2012 and then surging during 2014–2016. Therefore, we assumed that the build-up of ice from the accumulation of snowfall increasing in the reservoir area increased the driving stress, which led to higher ice creep rates and generated heat to produce meltwater, leading to reduced basal drag and faster sliding.

5.4 Glacier response to climate change

From the coldest years of the Little Ice Age, the areas of the glaciers at Malan were larger by 4.6% than for modern glaciers, compared with approximately 8% and 20% in Qangtang and TP, respectively (Pu et al., 2001). Thus, the glaciers in XM might be more stable. However, the warming trend from the 20th century was recorded from a Malan ice core, and the warmest period was between the 1950s and early 1980s. Several stable cold periods punctuated through the warming, especially between the late 1980s and 1990s, which may have been caused by a strong summer monsoon (Wang et al., 2003). Therefore, we speculated that the shrinkage of the glacier areas mainly occurred between 1970 and 1999 and could be a response to the warming of the 1950s to the early 1980s. In addition, a higher net accumulation rate was recorded between 1987 and 1995 from an ice core in Malan (Wang, 2009). Thus, the colder and wetter climate from the late 1980s to 1990s (Fig. 10) might have resulted in a slight negative or positive mass change for the glaciers during this period. This is likely the reason for the relatively small negative mass loss between 1970 and 1999.

Glacier area shrinkage (1970–1999) may lag behind the mass loss from the 1950s to the early 1980s in response to a warmer climate. With the rapid warming during the 21st century, glacier mass loss could be further accelerated. At the same time, glaciers have been observed to experience a slight area shrinkage from 2000 to 2018 relative to the colder climate from the late 1980s and into the 1990s. There was also low precipitation in XM and the slight increases in precipitation more recently have had very little impact on glacier change in the 21st century.

6 Conclusions

We investigated glacier area and mass changes for Mt. Xinqingfeng and Mt. Malan derived from topographic maps, Landsat, ASTER, SRTM DEM, and TerraSAR-X/TanDEM-X from ~1970 to 2018 and ~1970 to 2012, respectively. Our results showed that the glaciers experienced a small shrinkage from 641.2 ± 7.7 km^2 in 1970/71 to 613.9 ± 4.4 km^2 in 2018, corresponding to an area shrinkage of 4.3 ±1.4% (0.09 ± 0.03% a^{-1}) from 1970 to 2018. The shrinkage speed of the glacier area decreased after 2000 and the glacier area was stable after 2013, which can be mainly attributed to the advance or surge of some glaciers. However, the mass balances of glaciers at Xinqingfeng and Malan were negative at −0.22 ± 0.17 m w.e. a^{-1} and −0.29 ± 0.17 m w.e. a^{-1} from 1999 to 2012, respectively. A lower mass loss of 0.19 ± 0.14 m w.e. a^{-1} was found for the glaciers at Malan from 1970 to 1999 than from 1999-2012. Glacier variations at XM are heterogeneous and differ spatially as well as temporally. A total of seven glaciers showed surging or advancing from 1970 to 2018. Among them, the West Monuomaha Glacier, Monuomaha Glacier, and Zu Glacier were identified as surging glaciers, and the others may also be surging glaciers that required more evidence. These surge-type glaciers showed a long active period and comparatively low velocity, suggesting that thermal control was important for surge initiation and recession.

Author contributions. The concept of this study was developed by Zhen Zhang and Shiyin Liu. The digital elevation models were generated by Zhen Zhang and Zongli Jiang. Zhen Zhang performed the data analysis and wrote the draft of the paper. Zhen Zhang, Shiyin Liu and all other authors were involved in paper writing or supported this work.

Competing interests. The authors declare that they have no competing interests.

Acknowledgements. This research was supported by the Strategic Priority Research Program of the Chinese Academy of Sciences (Grant No. XDA19070501), The Ministry of Science and Technology (Grant No.2013FY111400), International Partnership Program of Chinese Academy of Sciences (Grant No. 131C11KYSB20160061), the National Natural Science Foundation of China (Grant Nos. 41701087, 41471067) and Research Funds Provided to New Recruitments of Yunnan University (YJRC3201702). Landsat, SRTM C-band and ASTER data were acquired from the US Geological Survey and NASA. The first and second glacier inventories were provided by a past MOST project (2006FY110200) (http://westdc.westgis.ac.cn/glacier). SRTM X-band and TerraSAR-X/TanDEM-X data were acquired from DLR. GoLIVE data were acquired from NSIDC (https://nsidc.org/data/NSIDC-0710/versions/1), And ITS_LIVE data were acuqired from NASA (https://its-live.jpl.nasa.gov/). We thank Etienne Berthier for guidance on uncertainty estimation of glacier elevation changes. We thank Shasha Zhang for preocessing data in revising our manuscript. And we also thank two anonymous reviewers and the scientific editor for their constructive comments on the manuscript.

References

Bahr, D. B. and Radić, V.: Significant contribution to total mass from very small glaciers, The Cryosphere, 6, 763-770, https://doi.org/ 10.5194/tc-6-763-2012, 2012.

Bao, W., Liu, S., Wei, J., and Guo, W.: Glacier changes during the past 40 years in the West Kunlun Shan, J Mt Sci-Engl, 12, 344-357, https://doi.org/10.1007/s11629-014-3220-0, 2015.

Berthier, E., Arnaud, Y., Vincent, C., and Rémy, F.: Biases of SRTM in high-mountain areas: Implications for the monitoring of glacier volume changes, Geophysical Research Letters, 33, L08502, https://doi.org/10.1029/2006gl025862, 2006.

Berthier, E., Cabot, V., Vincent, C., and Six, D.: Decadal Region-Wide and Glacier-Wide Mass Balances Derived from Multi-Temporal ASTER Satellite Digital Elevation Models. Validation over the Mont-Blanc Area, Frontiers in Earth Science, 4, https://doi.org/10.3389/feart.2016.00063, 2016.

Björnsson, H.: Hydrological characteristics of the drainage system beneath a surging glacier, Nature, 395, 771-774, https://doi.org/10.1038/27384, 1998.

Bolch, T., Pieczonka, T., and Benn, D. I.: Multi-decadal mass loss of glaciers in the Everest area (Nepal Himalaya) derived from stereo imagery, Cryosphere, 5, 349-358, https://doi.org/10.5194/tc-5-349-2011, 2011.

Bolch, T., Pieczonka, T., Mukherjee, K., and Shea, J.: Brief communication: Glaciers in the Hunza catchment (Karakoram) have been nearly in balance since the 1970s, The Cryosphere, 11, 531-539, https://doi.org/10.5194/tc-11-531-2017, 2017.

Brun, F., Berthier, E., Wagnon, P., Kaab, A., and Treichler, D.: A spatially resolved estimate of High Mountain Asia glacier mass balances, 2000-2016, Nat Geosci, 10, 668-673, https://doi.org/10.1038/NGEO2999, 2017.

Burgess, E. W., Forster, R. R., Larsen, C. F., and Braun, M.: Surge dynamics on Bering Glacier, Alaska, in 2008-2011, The Cryosphere, 6, 1251-1262, https://doi.org/10.5194/tc-6-1251-2012, 2012.

Chen, A. a., Wang, N., Li, Z., Wu, Y., Zhang, W., and Guo, Z.: Region-Wide Glacier Mass Budgets for the Tanggula Mountains between ~1969 and ~2015 Derived from Remote Sensing Data, Arctic, Antarctic, and Alpine Research, 49, 551-568, https://doi.org/10.1657/aaar0016-065, 2017.

Clarke, G. K. C., Collins, S. G., and Thompson, D. E.: Flow, Thermal Structure, and Subglacial Conditions of a Surge-Type Glacier, Canadian Journal of Earth Sciences, 21, 232-240, https://doi.org/10.1139/e84-024, 1984.

Costantini, M.: A Novel Phase Unwrapping Method Based on Network Programming, Ieee T Geosci Remote, 36, 813-821, https://doi.org/10.1109/36.673674, 1998.

Davis, C. H. and Poznyak, V. I.: The depth of penetration in Antarctic firn at 10 GHz, Ieee T Geosci Remote, 31, 1107-1111, https://doi.org/10.1109/36.263784, 1993.

Fahnestock, M., Scambos, T., Moon, T., Gardner, A., Haran, T., and Klinger, M.: Rapid large-area mapping of ice flow using Landsat 8, Remote Sensing of Environment, 185, 84-94, https://doi.org/10.1016/j.rse.2015.11.023, 2016.

Falaschi, D., Bolch, T., Lenzano, M. G., Tadono, T., Lo Vecchio, A., and Lenzano, L.: New evidence of glacier surges in the Central Andes of Argentina and Chile, Progress in Physical Geography: Earth and Environment, 42, 792-825, https://doi.org/10.1177/0309133318803014, 2018.

Farinotti, D., Longuevergne, L., Moholdt, G., Duethmann, D., Molg, T., Bolch, T., Vorogushyn, S., and Guntner, A.: Substantial glacier mass loss in the Tien Shan over the past 50 years, Nat Geosci, 8, 716-723, https://doi.org/10.1038/Ngeo2513, 2015.

Fischer, M., Huss, M., and Hoelzle, M.: Surface elevation and mass changes of all Swiss glaciers 1980–2010, The Cryosphere, 9, 525-540, https://doi.org/10.5194/tc-9-525-2015, 2015.

Fowler, A. C., Murray, T., and Ng, F. S. L.: Thermally controlled glacier surging, Journal of Glaciology, 47, 527-538, 2001.

Gardelle, J., Berthier, E., and Arnaud, Y.: Impact of resolution and radar penetration on glacier elevation changes computed from DEM differencing, Journal of Glaciology, 58, 419-422, https://doi.org/10.3189/2012jog11j175, 2012a.

Gardelle, J., Berthier, E., and Arnaud, Y.: Slight mass gain of Karakoram glaciers in the early twenty-first century, Nat Geosci, 5, 322-325, https://doi.org/10.1038/Ngeo1450, 2012b.

Gardelle, J., Berthier, E., Arnaud, Y., and Kääb, A.: Region-wide glacier mass balances over the Pamir-Karakoram-Himalaya during 1999-2011, The Cryosphere, 7, 1263–1286, https://doi.org/10.5194/tc-7-1263-2013, 2013.

Gardner, A. S., Moholdt, G., Cogley, J. G., Wouters, B., Arendt, A. A., Wahr, J., Berthier, E., Hock, R., Pfeffer, W. T., Kaser, G., Ligtenberg, S. R., Bolch, T., Sharp, M. J., Hagen, J. O., van den Broeke, M. R., and Paul, F.: A reconciled estimate of glacier contributions to sea level rise: 2003 to 2009, Science, 340, 852-857, https://doi.org/10.1126/science.1234532, 2013.

Gardner, A. S., Moholdt, G., Scambos, T., Fahnstock, M., Ligtenberg, S., van den Broeke, M., and Nilsson, J.: Increased West Antarctic and unchanged East Antarctic ice discharge over the last 7 years, The Cryosphere, 12, 521-547, https://doi.org/10.5194/tc-12-521-2018, 2018.

GB/T12343.1-2008: Compilation Specifications for National Fundamental Scale Mapse——Part 1: Compilation Specifications for 1:25000/1:50000/1:100000 Topographic Maps. General Administration of Quality Supervision Inspection and Quarantine, Beijing, 2008.

Guo, W., Liu, S., Xu, J., Wu, L., Shangguan, D., Yao, X., Wei, J., Bao, W., Yu, P., Liu, Q., and Jiang, Z.: The second Chinese glacier inventory: data, methods and results, Journal of Glaciology, 61, 357-372, https://doi.org/10.3189/2015JoG14J209, 2015.

Guo, W. Q., Liu, S. Y., Wei, J. F., and Bao, W. J.: The 2008/09 surge of central Yulinchuan glacier, northern Tibetan Plateau, as monitored by remote sensing, Annals of Glaciology, 54, 299-310, https://doi.org/10.3189/2013aog63a495, 2013.

Holzer, N., Vijay, S., Yao, T., Xu, B., Buchroithner, M., and Bolch, T.: Four decades of glacier variations at Muztagh Ata (eastern Pamir): a multi-sensor study including Hexagon KH-9 and Pléiades data, The Cryosphere, 9, 2071–2088, https://doi.org/10.5194/tc-9-2071-2015, 2015.

Huss, M.: Density assumptions for converting geodetic glacier volume change to mass change, The Cryosphere, 7, 877-887, https://doi.org/10.5194/tc-7-877-2013, 2013.

Immerzeel, W. W., van Beek, L. P., and Bierkens, M. F.: Climate change will affect the Asian water towers, Science, 328, 1382-1385, https://doi.org/10.1126/science.1183188, 2010.

Jiang, Z., Liu, S., Guo, W., li, J., Long, S., Wang, X., Wei, J., Zhang, Z., and Wu, K.: Recent surface elevation changes of three representative glaciers in Ányêmaqên Mountains, source region of Yellow River, Journal of Glaciology and Geocryology, 40, 231-237, https://doi.org/10.7522 /j.issn.1000-0240.2018.0027, 2018 (in Chinese with English abstract).

Kääb, A., Berthier, E., Nuth, C., Gardelle, J., and Arnaud, Y.: Contrasting patterns of early twenty-first-century glacier mass change in the Himalayas, Nature, 488, 495-498, https://doi.org/10.1038/nature11324, 2012.

Kääb, A., Treichler, D., Nuth, C., and Berthier, E.: Brief Communication: Contending estimates of 2003-2008 glacier mass balance over the Pamir–Karakoram–Himalaya, The Cryosphere, 9, 557-564, https://doi.org/10.5194/tc-9-557-2015, 2015.

Kamb, B., Raymond, C. F., Harrison, W. D., Engelhardt, H., Echelmeyer, K. A., Humphrey, N., Brugman, M. M., and Pfeffer, T.: Glacier Surge Mechanism - 1982-1983 Surge of Variegated Glacier, Alaska, Science, 227, 469-479, 1985.

Kamp, U., Bolch, T., and Olsenholler, J.: DEM generation from ASTER satellite data for geomorphometric analysis of Cerro Sillajhuay, Chile/Bolivia, ASPRS 2003 Annual Conference Proceedings, Anchorage, Alaska, 2003.

Kotlyakov, V. M., Rototaeva, O. V., and Nosenko, G. A.: The September 2002 Kolka Glacier Catastrophe in North Ossetia, Russian Federation: Evidence and Analysis, Mountain Research and Development, 24, 78-83, https://doi.org/10.1659/0276-4741(2004)024[0078:TSKGCI]2.0.CO2, 2004.

Krieger, G., Moreira, A., Fiedler, H., Hajnsek, I., Werner, M., Younis, M., and Zink, M.: TanDEM-X: A Satellite Formation for High-Resolution SAR Interferometry, Ieee T Geosci Remote, 45, 3317-3341, https://doi.org/10.1109/tgrs.2007.900693, 2007.

Lambrecht, A., Mayer, C., Wendt, A., Floricioiu, D., and Volksen, C.: Elevation change of Fedchenko Glacier, Pamir Mountains, from GNSS field measurements and TanDEM-X elevation models, with a focus on the upper glacier, Journal of Glaciology, 64, 637-648, https://doi.org/10.1017/jog.2018.52, 2018.

Li, B.: Nature Environment in the Hoh Xil Region of Qinghai, Science Press, Beijing, 1996.

Lin, H., Li, G., Cuo, L., Hooper, A., and Ye, Q.: A decreasing glacier mass balance gradient from the edge of the Upper Tarim Basin to the Karakoram during 2000-2014, Scientific reports, 7, 6712, https://doi.org/10.1038/s41598-017-07133-8, 2017.

Lingle, C. S. and Fatland, D. R.: Does englacial water storage drive temperate glacier surges?, Annals of Glaciology, 36, 14-20, https://doi.org/10.3189/172756403781816464, 2003.

Liu, L., Jiang, L., Jiang, H., Wang, H., Ma, N., and Xu, H.: Accelerated glacier mass loss (2011–2016) over the Puruogangri ice field in the inner Tibetan Plateau revealed by bistatic InSAR measurements, Remote Sensing of Environment, 231, 111241, https://doi.org/10.1016/j.rse.2019.111241, 2019.

Liu, Q., Guo, W., Nie, Y., Liu, S., and Xu, J.: Recent glacier and glacial lake changes and their interactions in the Bugyai Kangri, southeast Tibet, Annals of Glaciology, https://doi.org/10.3189/2016AoG71A415, 2015.

Motyka, R. J. and Truffer, M.: Hubbard Glacier, Alaska: 2002 closure and outburst of Russell Fjord and postflood conditions at Gilbert Point, Journal of Geophysical Research, 112, F02004, https://doi.org/10.5194/10.1029/2006jf000475, 2007.

Mukherjee, K., Bolch, T., Goerlich, F., Kutuzov, S., Osmonov, A., Pieczonka, T., and Shesterova, I.: Surge-Type Glaciers in the Tien Shan (Central Asia), Arctic, Antarctic, and Alpine Research, 49, 147-171, https://doi.org/10.1657/aaar0016-021, 2018..

Murray, T., Stuart, G. W., Miller, P. J., Woodward, J., Smith, A. M., Porter, P. R., and Jiskoot, H.: Glacier surge propagation by thermal evolution at the bed, Journal of Geophysical Research, 105, 13491, 2000.

Neckel, N., Braun, A., Kropáček, J., and Hochschild, V.: Recent mass balance of the Purogangri Ice Cap, central Tibetan Plateau, by means of differential X-band SAR interferometry, The Cryosphere, 7, 1623-1633, https://doi.org/10.5194/tc-7-1623-2013, 2013.

Neckel, N., Kropáček, J., Bolch, T., and Hochschild, V.: Glacier mass changes on the Tibetan Plateau 2003–2009 derived from ICESat laser altimetry measurements, Environmental Research Letters, 9, 1-7, https://doi.org/10.1088/1748-9326/9/1/014009, 2014.

Nuth, C. and Kääb, A.: Co-registration and bias corrections of satellite elevation data sets for quantifying glacier thickness change, The Cryosphere, 5, 271-290, https://doi.org/10.5194/tc-5-271-2011, 2011.

Pu, J., Yao, T., Wang, N., Ding, L., and Zhang, Q.: Recent Variation of the Malan Glacier in Hoh Xil Region of the Tibetan Plateau, Journal of Glaciology and Geocryology, 23, 189-192, 2001 (in Chinese with English abstract).

Qiao, C.: Remote Sensing Monitoring of Glacier Changes in Dongkemadi Region of Tanggula Mountain, Journal of Anhui Agricultural Sciences, 38, 7703-7705, 2010 (in Chinese with English abstract).

Quincey, D. J., Glasser, N. F., Cook, S. J., and Luckman, A.: Heterogeneity in Karakoram glacier surges, Journal of Geophysical Research: Earth Surface, 120, 1288-1300, https://doi.org/10.1002/2015jf003515, 2015.

Round, V., Leinss, S., Huss, M., Haemmig, C., and Hajnsek, I.: Surge dynamics and lake outbursts of Kyagar Glacier, Karakoram, The Cryosphere, 11, 723-739, https://doi.org/10.5194/tc-11-723-2017, 2017.

Sakai, A., Nuimura, T., Fujita, K., Takenaka, S., Nagai, H., and Lamsal, D.: Climate regime of Asian glaciers revealed by GAMDAM glacier inventory, The Cryosphere, 9, 865-880, https://doi.org/10.5194/tc-9-865-2015, 2015.

Sam, L., Bhardwaj, A., Kumar, R., Buchroithner, M. F., and Martin-Torres, F. J.: Heterogeneity in topographic control on velocities of Western Himalayan glaciers, Scientific reports, 8, 12843, https://doi.org/10.1038/s41598-018-31310-y, 2018.

Sevestre, H. and Benn, D. I.: Climatic and geometric controls on the global distribution of surge-type glaciers: implications for a unifying model of surging, Journal of Glaciology, 61, 646-662, https://doi.org/10.3189/2015JoG14J136, 2015.

Sevestre, H., Benn, D. I., Hulton, N. R. J., and Baelum, K.: Thermal structure of Svalbard glaciers and implications for thermal switch models of glacier surging, Journal of Geophysical Research: Earth Surface, 120, 2220-2236, https://doi.org/10.1002/2015jf003517, 2015.

Shangguan, D. H., Bolch, T., Ding, Y. J., Kröhnert, M., Pieczonka, T., Wetzel, H. U., and Liu, S. Y.: Mass changes of Southern and Northern Inylchek Glacier, Central Tian Shan, Kyrgyzstan, during ~1975 and 2007 derived from remote sensing data, The Cryosphere, 9, 703-717, https://doi.org/10.5194/tc-9-703-2015, 2015.

Sun, M., Liu, S., Yao, X., Guo, W., and Xu, J.: Glacier changes in the Qilian Mountains in the past half-century: Based on the revised First and Second Chinese Glacier Inventory, J Geogr Sci, 28, 206-220, https://doi.org/10.1007/s11442-018-1468-y, 2018.

Surdyk, S.: Using microwave brightness temperature to detect short-term surface air temperature changes in Antarctica: An analytical approach, Remote Sensing of Environment, 80, 256-271, https://doi.org/10.1016/S0034-4257(01)00308-X, 2002.

Wang, D. and Käab, A.: Modeling Glacier Elevation Change from DEM Time Series, Remote Sensing, 7, 10117-10142, https://doi.org/10.3390/rs70810117, 2015.

Wang, H., Hu, J., Tan, q., and Xu, X.: Evaluation of the contour line interpolation generated DEMs of mountainous area in north China, Contributions to Geology and Mineral Resources Reserarch, 29, 433-437, https://10.60.6053/j.issn.1001-1412.2014.03.019, 2014 (in Chinese with English abstract).

Wang, N.: Variations in net accumulation rate of the malan ice core from the northern tibetan plateau over the period of 1887 though 1998 and their relationship to solar activity, Quaternary Sciences, 29, 913-919, 2009 (in Chinese with English abstract).

Wang, Y., Pu, J., Zhang, Y., and Sun, W.: Characteristic of Present Warming Change Recorded in Malan Ice Core, Central Tibetan Plateau, Journal of Glaciology and Geocryology, 25, 130-134, 2003 (in Chinese with English abstract).

Wang, Y., Wu, L., Xu, J., and Liu, S.: Variation and uncertainty analysis of the glaciers in the past 50 years in Geladandong of Tibetan Plateau, Journal of Glaciology and Geocryology, 35, 255-262, 2013 (in Chinese with English abstract).

Wei, J., Liu, S., Guo, W., Xu, J., Bao, W., and Shangguan, D.: Changes in Glacier Volume in the North Bank of the Bangong Co Basin from 1968 to 2007 Based on Historical Topographic Maps, SRTM, and ASTER Stereo Images, Arctic, Antarctic, and Alpine Research, 47, 301-311, https://doi.org/10.1657/aaar00c-13-129, 2015a.

Wei, J., Liu, S., Xu, J., Guo, W., Bao, W., Shangguan, D., and Jiang, Z.: Mass Loss from Glaciers in the Chinese Altai Mountains between 1959 and 2008 Revealed Based on Historical Maps, SRTM, and ASTER Images, J Mt Sci-Engl, 12, 330-343, https://doi.org/10.1007/s11629-014-3175-1, 2015b.

Wei, J. F., Liu, S. Y., Guo, W. Q., Yao, X. J., Xu, J. L., Bao, W. J., and Jiang, Z. L.: Surface-area changes of glaciers in the Tibetan Plateau interior area since the 1970s using recent Landsat images and historical maps, Annals of Glaciology, 55, 213-222, https://doi.org/10.3189/2014aog66a038, 2014.

Wu, K., Liu, S., Guo, W., Wei, J., Xu, J., Bao, W., and Yao, X.: Glcier change in the western Nyainqentanglha Range, Tibetan Plateau using historical maps and Landsat imagery:1970-2014, J Mt Sci-Engl, 13, 1358-1374, https://doi.org/10.1007/s11629-0163997-0, 2016.

Wu, K., Liu, S., Jiang, Z., Xu, J., Wei, J., and Guo, W.: Recent glacier mass balance and area changes in the Kangri Karpo Mountains from DEMs and glacier inventories, The Cryosphere, 12, 103-121, https://doi.org/10.5194/tc-12-103-2018, 2018.

Xie, Z., Han, J., Feng, Q., and Wang, X.: Primary Study on the Glaciers of Mountain Malan, Hoh Xil Region, Qinghai-Xizang Plateau, Journal of Natural Science of Hunan Normal University, 23, 83-88, 2000 (in Chinese with English abstract).

Xu, J., Shangguan, D., and Wang, J.: Three-Dimensional Glacier Changes in Geladandong Peak Region in the Central Tibetan Plateau, Water, 10, 1749, https://doi.org/10.3390/w10121749, 2018.

Yao, T. D., Thompson, L., Yang, W., Yu, W. S., Gao, Y., Guo, X. J., Yang, X. X., Duan, K. Q., Zhao, H. B., Xu, B. Q., Pu, J. C., Lu, A. X., Xiang, Y., Kattel, D. B., and Joswiak, D.: Different glacier status with atmospheric circulations in Tibetan Plateau and surroundings, Nat Clim Change, 2, 663-667, https://doi.org/10.1038/Nclimate1580, 2012.

Yao, X., Liu, S., Zhu, Y., Gong, P., An, L., and Li, X.: Design and implementation of an automatic method for deriving glacier centerlines based on GIS, Journal of Glaciology and Geocryology, 37, 1563-1570, https://doi.org/10.7522/j.issn.1000-0240.2015.0173, 2015 (in Chinese with English abstract).

Ye, Q., Zong, J., Tian, L., Cogley, J. G., Song, C., and Guo, W.: Glacier changes on the Tibetan Plateau derived from Landsat imagery: mid-1970s – 2000–13, Journal of Glaciology, 63, 273-287, https://doi.org/10.1017/jog.2016.137, 2017.

Zhang, W.: A Surging Glacier in the Nanjiabawa Peak Area, Himalayas, Journal of Glaciology and Geocryology, 5, 75-76, 1983 (in Chinese with English abstract).

Zhang, Z. and Liu, S.: Area changes and mass balance of glaciers in KangzhagRi of the Tibetan Plateau from 1970 to 2016 as derived from remote Sensing data, Journal of Geo-information Science, 20, 1338-1349, https://doi.org/10.12082/dqxxkx.2018.180059, 2018 (in Chinese with English abstract).

Zhang, Z., Liu, S., Wei, J., Xu, J., Guo, W., Bao, W., and Jiang, Z.: Mass Change of Glaciers in Muztag Ata-Kongur Tagh, Eastern Pamir, China from 1971/76 to 2013/14 as Derived from Remote Sensing Data, PloS one, 11, e0147327, https://doi.org/10.1371/journal.pone.0147327, 2016.

Zhang, Z., Liu, S., Zhang, Y., Wei, J., Jiang, Z., and Wu, K.: Glacier variations at Aru Co in western Tibet from 1971 to 2016 derived from remote-sensing data, Journal of Glaciology, 64, 397-406, https://doi.org/10.1017/jog.2018.34, 2018.

Zhou, Y. S., Hu, J., Li, Z. W., Li, J., Zhao, R., and Ding, X. L.: Quantifying glacier mass change and its contribution to lake growths in central Kunlun during 2000-2015 from multi-source remote sensing data, Journal of Hydrology, 570, 38-50, https://doi.org/10.1177/0309133318803014, 2019.

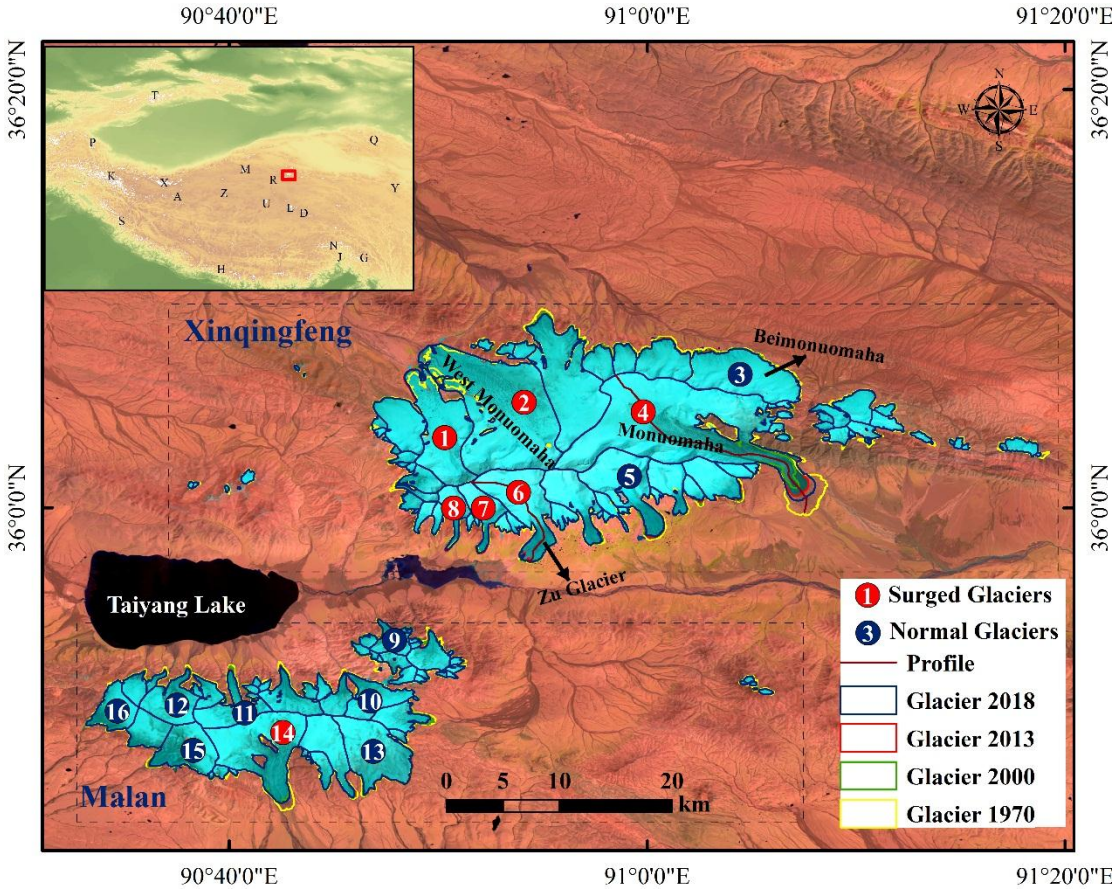

Figure 1. Overview of the Xinqingfeng and Malan glaciers (Background image: Landsat 8 OLI of 31 July 2013, A: Aru Co, D: Dongkemadi, G: Kangri Karpo, H: Himalayas, J: Namjagbarwa, K: Karakoram, L: Geladandong, M:Ulugh Muztagh, N: Nyainqentanglha, P: Pamir, Q: Qilian, R: Kangzhag Ri, S: Spiti Lahaul, T: Tien Shan, U: Purogangri, X: West Kunlun, Y: Ányêmaqên, Z: Zangsar Kangri).

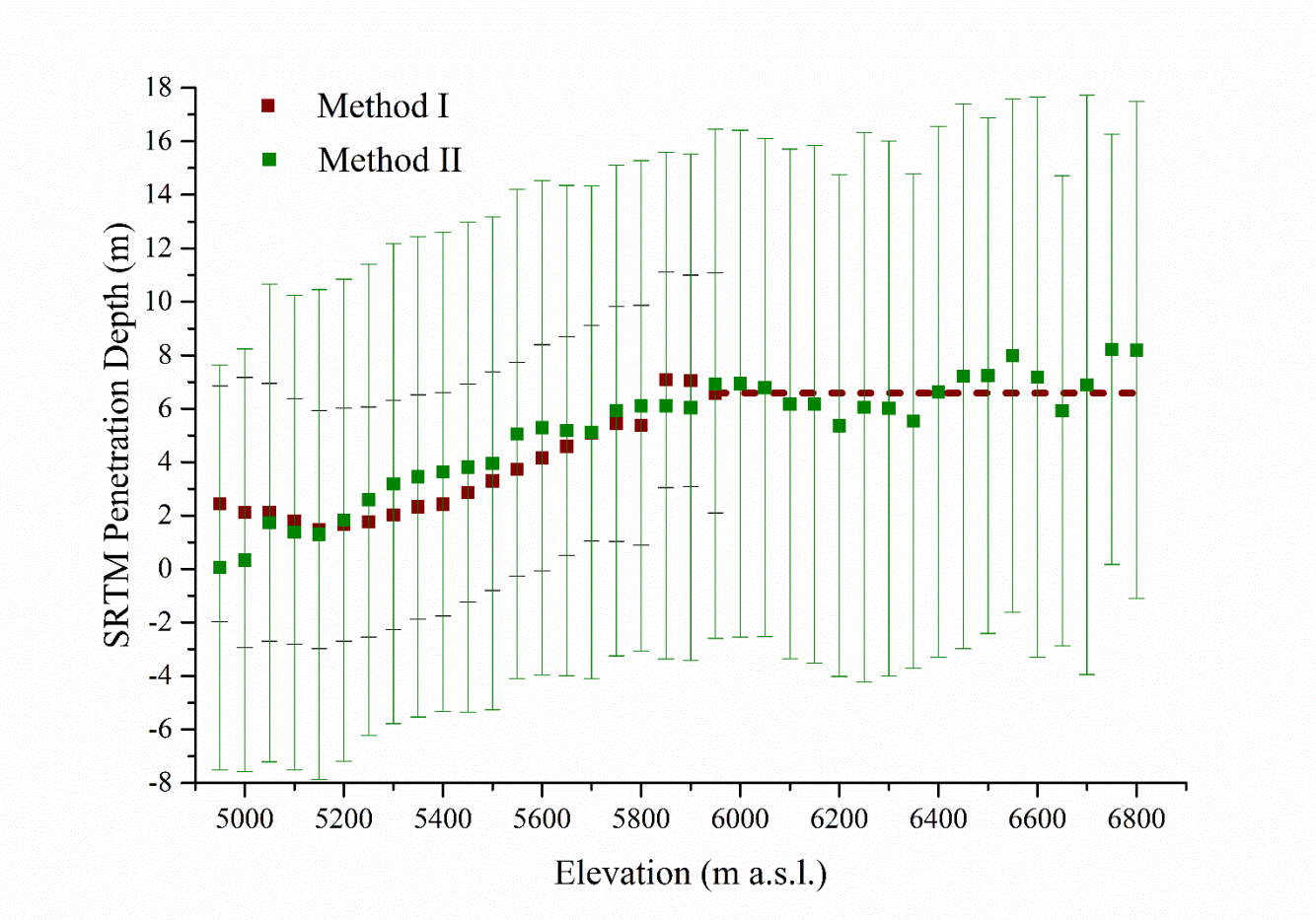

Figure 2. Estimation of the penetration depth of SRTM-C radar signal by the differences between SRTM-C and SRTM-X DEM with assuming no penetration of SRTM-X (Method I) and linearly extrapolated dh/dt of correctional ASTER DEMs (Method II).

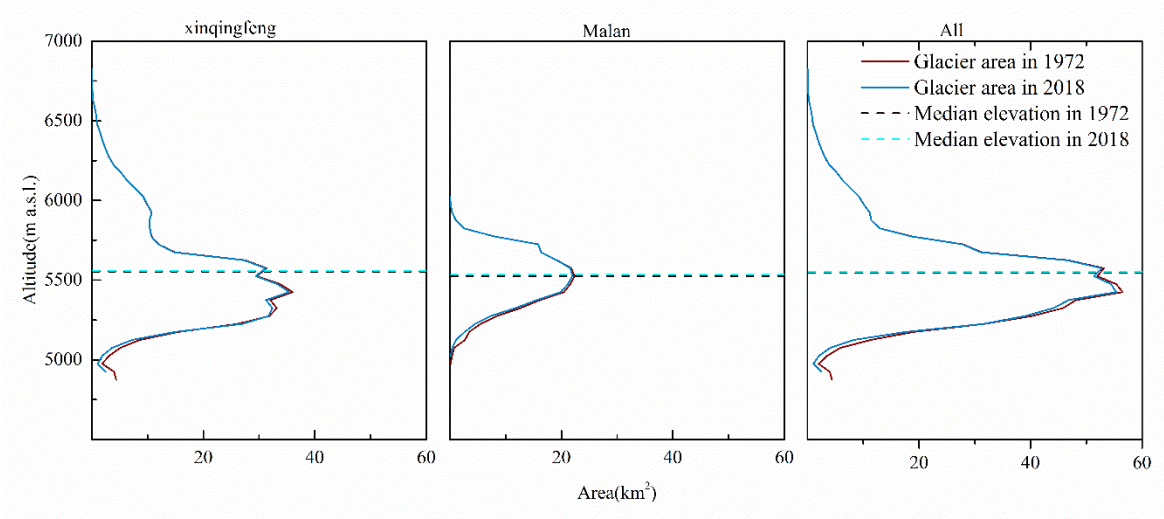

Figure 3. Hypsography of glaciers in 1970/71 and 2018.

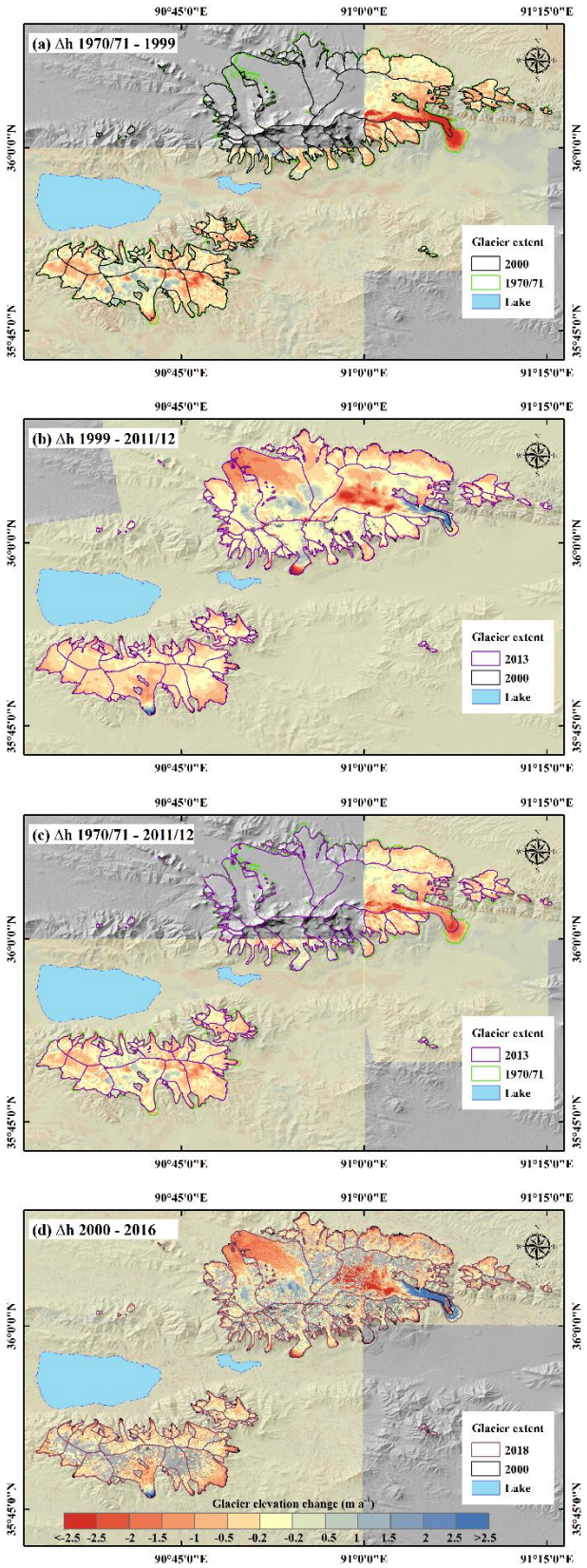

Figure 4. Elevation change of glaciers in XM during 1970/71-1999 (a), 1999-2011/12 (b), 1970/71-2011/12 (c) and 2000-2016 (d). The data of Fig. 4 (d) was derived from Brun et al. (2017).

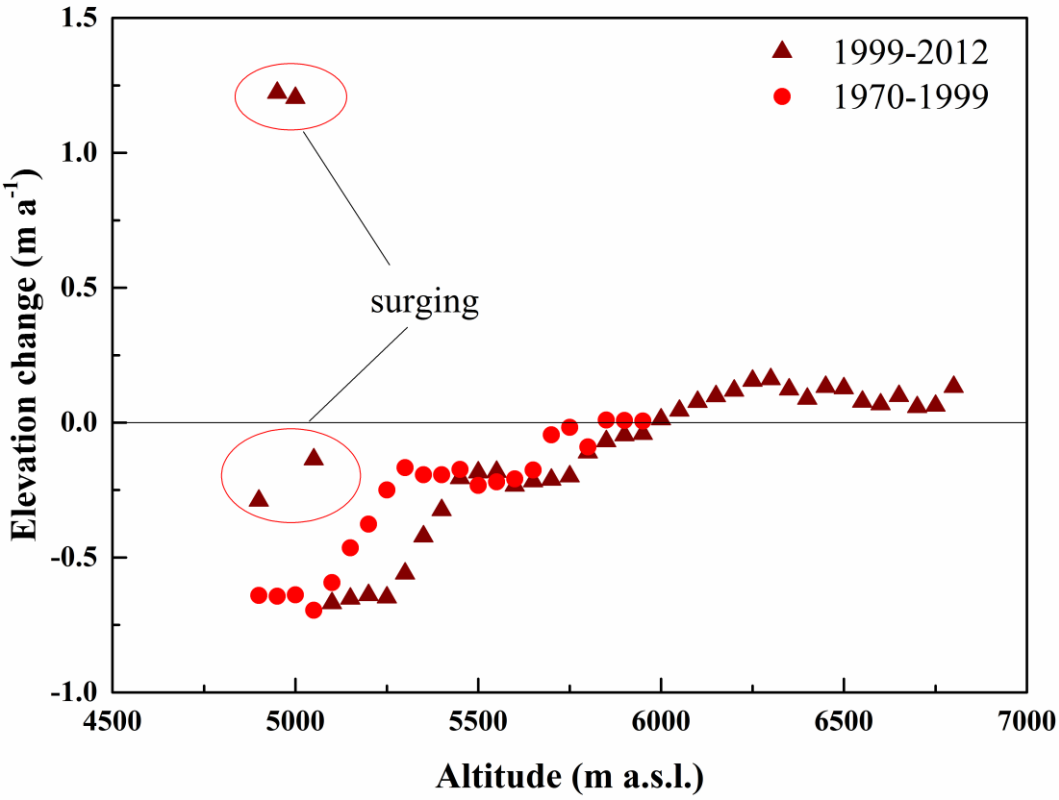

Fig. 5: Altitude distributions of glacier thickness change separated into 50 m elevation bins between 1970-1999 and 1999-2012.

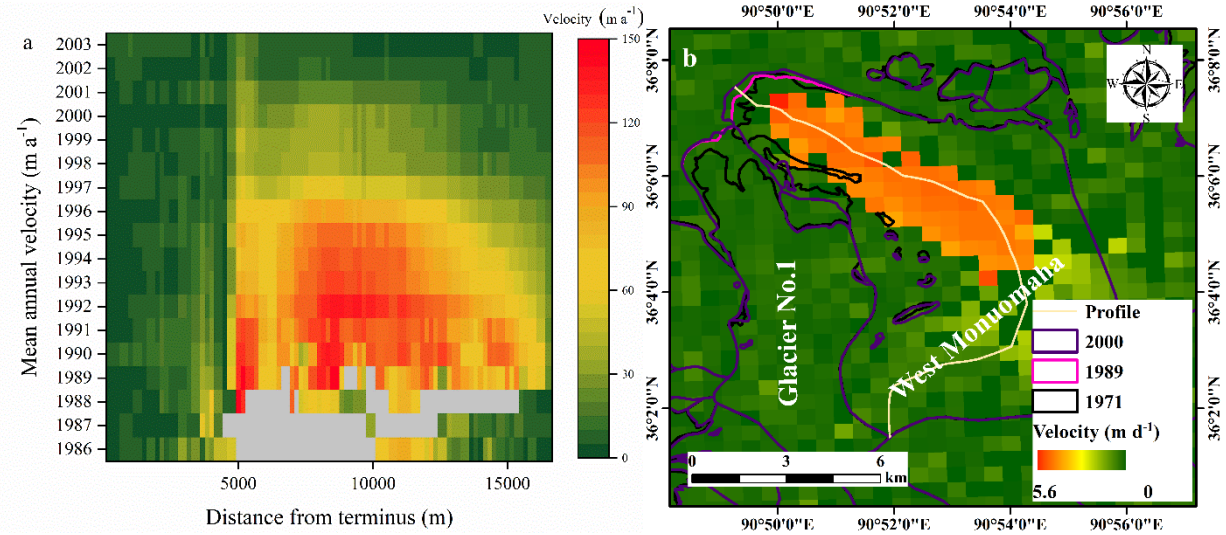

Figure 6. Panel (a) shows centre line annual velocity profiles from 1986-2003. (b) shows this glacier had a higher velocity from 12 October, 1987 to 29 Novermber, 1987 with a maximum velocity of 5.6 m d^{-1}.

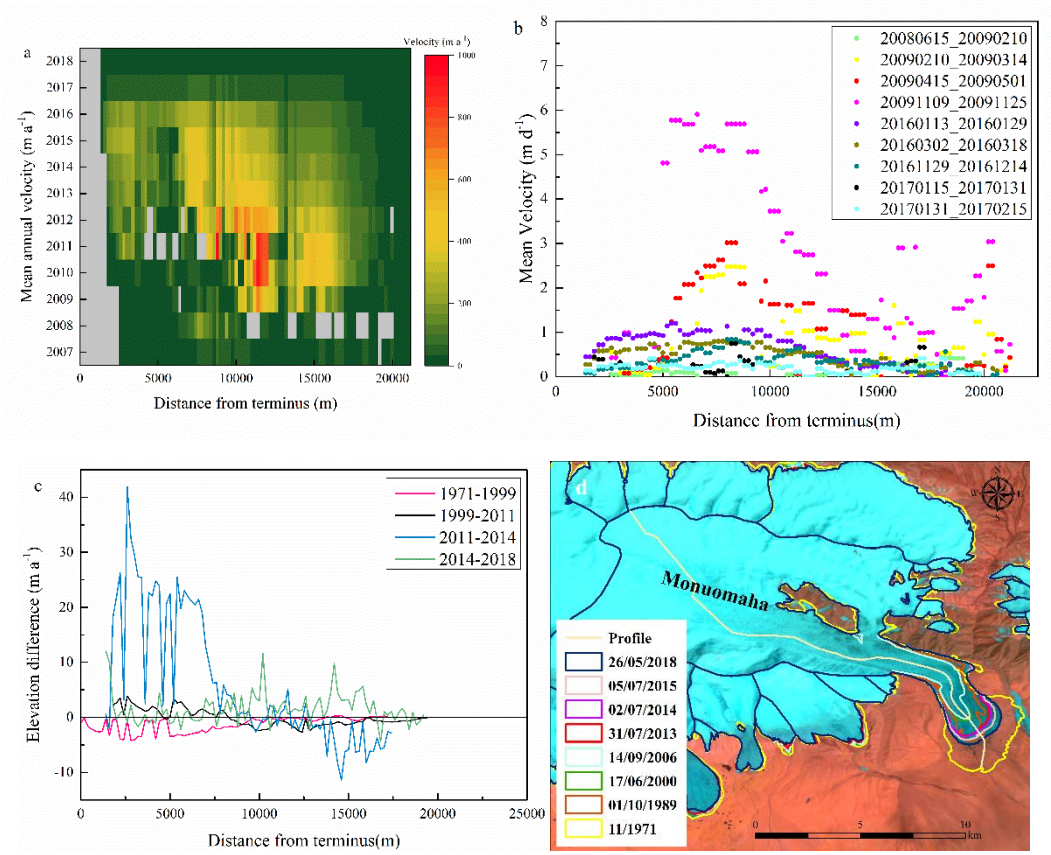

Figure 7. Panel (a) shows centre line annual velocity profiles from 2007-2018. (b) shows specific entre line velocity profiles with supplementary for (a). (c) shows profiles of Monuomaha Glacier during different periods. The entre line profiles, derived from TOPO DEM data. (d) shows glacier terminus change. Background image from Landsat 8 OLI of 26 May 2018.

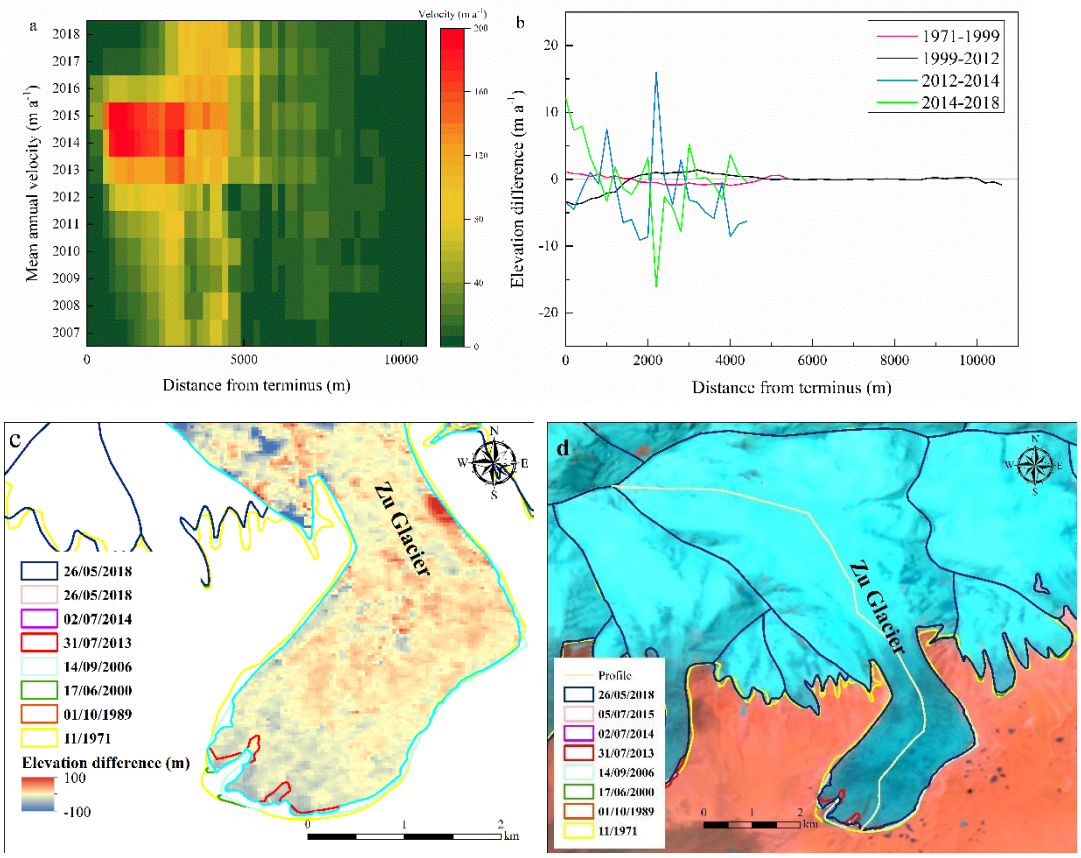

Figure 8. Panels (a) shows centre line annual velocity profiles from 2007-2018. (b) shows profiles of Monuomaha Glacier during different periods. (c) shows the elevation difference from 2014 to 2018. The profiles, derived from TOPO DEM data. (d) shows glacier terminus change. Background image from Landsat 8 OLI of 26 May 2018.

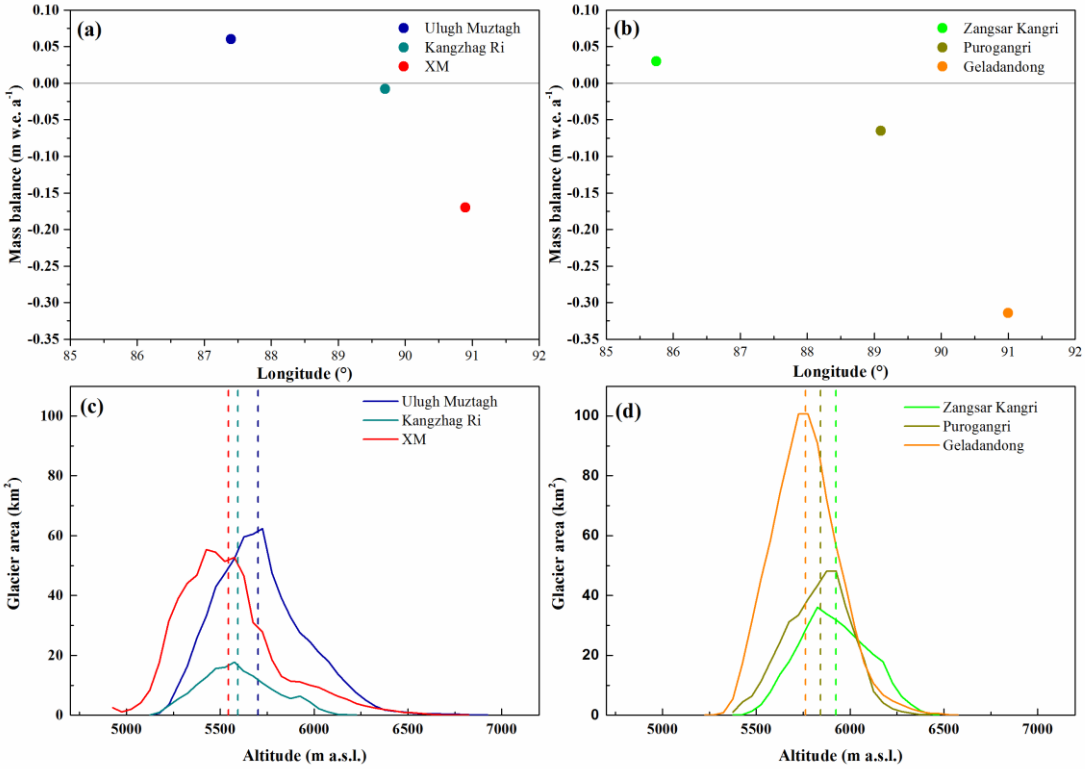

Figure 9. (a) Glacier mass balance in glacial clusters along approximately 35.5–36.5 °N, from 87 °E to 91 °E (Ulugh Muztagh, Kangzhag Ri, and XM). (b) Glacier mass balance in glacial clusters (Zangsar Kangri, Purogangri, and Geladandong) along approximately 33–34.5 °N, from 85.3 °E to 91.5 °E. (c-d) Hypsography of glacier for six clusters. Diferent colours indicate diferent clusters. The vertical dashed lines indicate their mean median elevation.

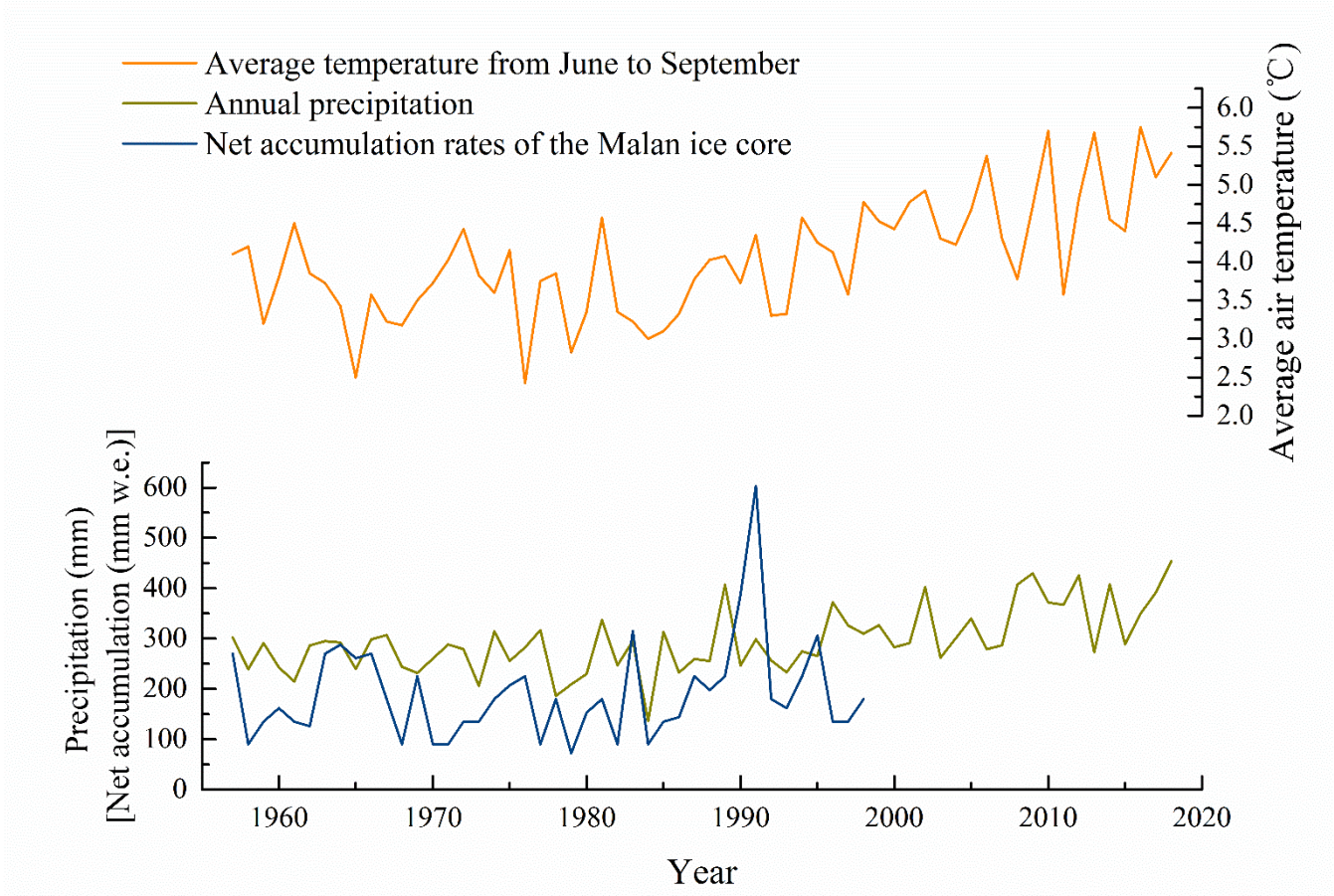

Figure 10. Changes in the average air temperature (from June to September) and annual precipitation during 1957–2018 recorded at the Wudaoliang station. And the net accumulation recorded from Malan ice core.

Table 1. Detailed information about the data used in this study

Source	Acquisition date	Space Resolution (m)	Usage
TerraSAR-X/TanDEM-X	8 Mar 2011 5 Mar 2012 16 Mar 2012 29 Apr 2012	12	Estimation of glacier elevation change
Topographic maps	Oct 1970 Jan 1971 Nov 1971 Dec 1971		Glacier identification
TOPO DEMs	Oct 1970 Nov 1971 Dec 1971	15	Estimation of glacier elevation change
ASTER DEMS (AST14DMO)	2000-2018	15	Estimation of glacier elevation change
SRTM DEM (C-band and X-band)	11-22 Feb 2000	30	Estimation of glacier elevation change
Landsat 1~3/MSS	1972~1976	79	Glacier identification
Landsat 5/TM	1986~2011	30	Glacier identification
Landsat 7/ETM+	2000~2012	Pan: 15; MS: 30	Glacier identification
Landsat 8/OLI	2013~2018	Pan: 15; MS: 30	Glacier identification
GoLIVE	2013~2018	300	Glacier velocity
ITS_LIVE	1986-2018	480	Glacier velocity

Table 2. The C band radar penetration depth caculating by three methods and comparsion with Zhou et al. (2009).

Item	Xinqingfeng	Malan	Total
Method 1	3.74	3.58	3.69
Method 2	4.42	4.45	4.43
Method 3			3.66
Zhou et al. (2019)	3.43	3.26	

Table 3. Statistics of errors of elevation difference at off-glacier region between the TOPO, SRTM and TSX/TDX. MEAN is mean elevation difference, STDV is standard deviation.

Item	MEAN (m)	STDV (m)	MIN (m)	MAX (m)
SRTM-TOPO	0.49	10.20	-91.12	96.40
TSX/TDX - SRTM	-0.68	5.95	-46.32	54.31
TSX/TDX-TOPO	-0.63	10.57	-50.85	33.23

Table 4. Glacier area (A) and changes (ΔA) from 1970−2018 for selected glaciers that have mass−balance estimates and for all glaciers of the study area.

Region	ID	GLIMS ID	A_{1970} (km^2)	1970−2000			2000−2013			1970−2013			2013−2018			1970−2018		
				ΔA (km^2)	ΔA (%)	Rate (% a^{-1})	ΔA (km^2)	ΔA (%)	Rate (% a^{-1})	ΔA (km^2)	ΔA (%)	Rate (% a^{-1})	ΔA (km^2)	ΔA (%)	Rate (% a^{-1})	ΔA (km^2)	ΔA (%)	Rate (% a^{-1})
Xinqingfeng	1	G090837E36060N	26.7	1.9	7.2	0.23	−0.4	−1.4	−0.11	1.5	5.5	0.13	−0.2	−0.6	−0.11	1.4	4.9	0.11
	2	G090884E36076N	66.6	2.4	3.6	0.12	−0.4	−0.6	−0.05	2.0	2.9	0.07	−0.0	−0.0	−0.00	2.0	2.9	0.06
	3	G091076E36106N	27.2	−1.0	−3.5	−0.12	−0.5	−1.9	−0.15	−1.5	−5.6	−0.13	−0.0	−0.2	−0.03	−1.5	−5.8	−0.12
	4	G091032E36060N	94.8	−10.8	−11.4	−0.40	3.6	4.3	0.33	−7.2	−8.2	−0.18	1.5	1.7	0.34	−5.7	−6.4	−0.13
	5	G090983E36018N	22.2	−0.6	−2.6	−0.09	−0.2	−1.1	−0.09	−0.8	−3.9	−0.09	−0.2	−0.8	−0.17	−1.0	−4.7	−0.10
	6	G090901E36002N	23.3	−0.4	−1.5	−0.05	−0.3	−1.2	−0.09	−0.6	−2.8	−0.06	0.1	0.3	0.06	−0.5	−2.1	−0.04
	7	G090868E35998N	8.5	−0.2	−2.4	−0.08	0.1	1.1	0.08	−0.1	−1.4	−0.03	−0.1	−1.0	−0.19	−0.2	−2.4	−0.05
	8	G090846E36001N	5.7	0.0	0.7	0.02	0.0	0.6	0.05	0.1	1.3	0.03	−0.0	−0.6	−0.12	0.0	0.7	0.02
subtotal			443.0	−16.9	−3.8	−0.13	−0.2	−0.0	−0.00	−17.1	−3.9	−0.09	0.5	0.1	0.02	−16.6	−3.7	−0.08
Malan	9	G090796E35893N	5.3	−0.0	−0.8	−0.03	−0.0	−0.7	−0.06	−0.1	−1.5	−0.04	−0.1	−1.2	−0.25	−0.1	−2.8	−0.06
	10	G090781E35848N	10.5	−0.4	−3.9	−0.13	−0.0	−0.0	−0.00	−0.4	−4.0	−0.09	−0.0	−0.3	−0.07	−0.4	−4.4	−0.09
	11	G090668E35840N	10.9	−0.3	−2.9	−0.10	−0.1	−1.2	−0.09	−0.4	−4.3	−0.10	−0.0	−0.2	−0.03	−0.5	−4.4	−0.09
	12	G090621E35846N	12.1	−0.4	−3.3	−0.11	−0.1	−0.7	−0.06	−0.5	−4.2	−0.09	−0.0	−0.4	−0.07	−0.5	−4.5	−0.09
	13	G090782E35805N	23.0	−0.4	−1.8	−0.06	−0.3	−1.1	−0.09	−0.7	−3.0	−0.07	−0.2	−0.9	−0.17	−0.9	−3.8	−0.08
	14	G090693E35807N	32.2	−1.7	−5.1	−0.18	0.2	0.6	0.05	−1.5	−4.8	−0.11	0.0	0.0	0.00	−1.5	−4.8	−0.10

	15	G090633E35808N	14.5	−0.2	−1.3	−0.04	−0.1	−0.5	−0.04	−0.3	−1.8	−0.04	−0.0	−0.2	−0.03	−0.3	−2.0	−0.04
	16	G090575E35839N	9.2	−0.2	−2.2	−0.07	−0.0	−0.5	−0.04	−0.3	−2.8	−0.06	−0.0	−0.1	−0.02	−0.3	−2.9	−0.06
subtotal			198.2	−7.9	−4.0	−0.14	−2.2	−1.2	−0.09	−10.1	−5.1	−0.12	−0.7	−0.4	−0.07	−10.8	−5.4	−0.11
total			641.2	−24.8	−3.9	−0.13	−2.3	−0.4	−0.03	−27.2	−4.2	−0.10	−0.2	−0.0	−0.01	−27.4	−4.3	−0.09

Table 5. Glacier length (L) and changes (ΔL) at Xinqingfeng and Malan for selected glaciers.

Region	ID	GLIMS ID	$L_{1970/71}$ (km)	$\Delta L_{1970/71\text{-}2000}$ (m)	$\Delta L_{2000\text{-}2013}$ (m)	$\Delta L_{2013\text{-}2018}$ (m)	$\Delta L_{1970/71\text{-}2018}$ (m)
Xinqingfeng	1	G090837E36060N	12.05 ± 0.01	329.3 ± 20.2	0.0 ± 16.8	−83.2 ± 10.6	246.1 ± 15.4
	2	G090884E36076N	15.36 ± 0.01	584.8 ± 20.2	0.0 ± 16.8	0.0 ±10.6	584.8 ± 15.4
	3	G091076E36106N	9.67 ± 0.01	−52.9 ± 20.2	0.0 ± 16.8	0.0 ± 10.6	−52.9 ± 15.4
	4	G091032E36060N	20.98 ± 0.01	−2546.8 ± 20.2	650.5 ± 16.8	513.5 ± 10.6	−1382.8 ± 15.4
	5	G090983E36018N	9.50 ± 0.01	−169.1 ± 20.2	−55.0 ± 16.8	−216.4 ± 10.6	−440.5 ± 15.4
	6	G090901E36002N	10.80 ± 0.01	−45.0 ± 20.2	−46.8 ± 16.8	46.0 ± 10.6	−45.8 ± 15.4
	7	G090868E35998N	6.90 ± 0.01	40.8 ± 20.2	107.8 ± 16.8	−43.4 ± 10.6	105.2 ± 15.4
	8	G090846E36001N	5.78 ± 0.01	432.0 ± 20.2	−19.7 ± 16.8	−75.7 ± 10.6	336.6 ± 15.4
	Selected glaciers (mean)			−178.4 ± 20.2	79.6 ± 16.8	17.6 ± 10.6	−81.2 ± 15.4
	Selected glaciers (mean annual)			−5.9 ± 0.7	6.1 ± 1.3	3.5 ± 2.1	−1.7 ± 0.3
Malan	9	G090796E35893N	3.87 ± 0.01	0 ± 20.2	−44.5 ± 16.8	−37.8 ± 10.6	−82.3 ± 15.4
	10	G090781E35848N	5.20 ± 0.01	−89.3 ± 20.2	−17.6 ± 16.8	−9.7 ± 10.6	−116.6 ± 15.4
	11	G090668E35840N	5.13 ± 0.01	−121.6 ± 20.2	−306.2 ± 16.8	−78.1 ± 10.6	−505.9 ± 15.4
	12	G090621E35846N	6.01 ± 0.01	−220.5 ± 20.2	−75.4 ± 16.8	−51.6 ± 10.6	−347.5 ± 15.4
	13	G090782E35805N	8.61 ± 0.01	−55.5 ± 20.2	−82.8 ± 16.8	−26.1 ± 10.6	−164.4 ± 15.4
	14	G090693E35807N	9.18 ± 0.01	−873.9 ± 20.2	183.4 ± 16.8	0.0 ± 10.6	−690.5 ± 15.4
	15	G090633E35808N	5.81 ± 0.01	−60.0 ± 20.2	−72.7 ± 16.8	−54.9 ± 10.6	−187.6 ± 15.4
	16	G090575E35839N	4.28 ± 0.01	−10.9 ± 20.2	−35.6 ± 16.8	−14.8 ± 10.6	−61.3 ± 15.4
	Selected glaciers (mean)			−179.0 ± 20.2	−56.4 ± 16.8	−56.4 ± 10.6	−269.5 ± 15.4
	Selected glaciers (mean annual)			−6.0 ± 0.7	−4.3 ± 1.3	−11.3 ± 2.1	−5.6 ± 0.3
Total	Selected glaciers (mean)			−178.7 ± 20.2	11.6 ± 16.8	−8.3 ± 10.6	−175.3 ± 15.4
	Selected glaciers (mean annual)			−6.0 ± 0.7	0.9 ± 1.3	−1.7 ± 2.1	−3.7 ± 0.3

Table 6. Glacier mean elevation (ΔH) and geodetic glacier mass balance rates measured from DEM differencing.

Region	ID	GLIMS ID	1970/71−1999		1999−2011/12		1970/71−2011/12		2000−2016*
			Mean ΔH (m)	Annual mass balance (m w.e. a^{-1})	Mean ΔH (m)	Annual mass balance (m w.e. a^{-1})	Mean ΔH (m)	Annual mass balance (m w.e. a^{-1})	Annual mass balance (m w.e. a^{-1})
Xinqingfeng	1	G090837E36060N			−4.41 ± 2.26	−0.29 ± 0.18			−0.22
	2	G090884E36076N			−5.97 ± 2.32	−0.39 ± 0.18			−0.33
	3	G091076E36106N	−4.44 ± 2.75	−0.13 ± 0.09	−4.41 ± 2.00	−0.31 ± 0.15	−8.65 ± 0.91	−0.17 ± 0.02	−0.40
	4	G091032E36060N			−4.77 ± 2.16	−0.35 ± 0.17			−0.02
	5	G090983E36018N			1.43 ± 2.11	0.10 ± 0.16			0.04
	6	G090901E36002N			1.02 ± 2.12	0.07 ± 0.16			0.05
	7	G090868E35998N			0.15 ± 2.09	0.01 ± 0.16			0.02
	8	G090846E36001N			−0.35 ± 2.00	−0.02 ± 0.15			0.04
subtotal					−3.50 ± 2.17	−0.22 ± 0.17			−0.14
Malan	9	G090796E35893N	−3.21 ± 3.71	−0.09 ± 0.13	−4.41 ± 2.15	−0.29 ± 0.17	−7.85 ± 0.84	−0.16 ± 0.02	−0.20
	10	G090781E35848N	−7.17 ± 3.48	−0.21 ± 0.12	−3.96 ± 2.11	−0.26 ± 0.17	−10.40 ± 0.85	−0.21 ± 0.02	−0.25
	11	G090668E35840N	−8.00 ± 3.90	−0.23 ± 0.13	−2.79 ± 2.25	−0.18 ± 0.18	−10.85 ± 0.81	−0.22 ± 0.02	−0.08
	12	G090621E35846N	−12.37 ± 4.28	−0.36 ± 0.15	−4.72 ± 2.24	−0.31 ± 0.18	−18.65 ± 0.81	−0.38 ± 0.02	−0.27
	13	G090782E35805N	−16.41 ± 3.89	−0.48 ± 0.13	−5.22 ± 2.23	−0.34 ± 0.18	−20.99 ± 0.83	−0.42 ± 0.02	−0.39
	14	G090693E35807N	0.84 ± 3.96	0.02 ± 0.14	−4.36 ± 2.25	−0.29 ± 0.18	−3.35 ± 0.81	−0.07 ± 0.02	−0.17
	15	G090633E35808N	0.04 ± 4.49	0.00 ± 0.15	−5.26 ± 2.33	−0.34 ± 0.18	−5.71 ± 0.80	−0.12± 0.02	−0.14
	16	G090575E35839N	−9.46 ± 3.86	−0.28 ± 0.13	−5.92 ± 2.12	−0.39 ± 0.17	−13.47 ± 0.84	−0.27± 0.02	−0.39
subtotal			−6.53 ± 3.95	−0.19 ± 0.14	−4.42 ± 2.21	−0.29 ± 0.17	−10.72 ± 0.91	−0.22 ± 0.02	−0.23
total					−3.78 ± 2.18	−0.24 ± 0.17			−0.17

*These results were derived from Brun et al. (2017).

Table 7. Main characteristics of surging or advancing glaciers.

Region	ID	GLIMS ID	Advance period	Advance (m)	Advance rate (m a^{-1})	Relatiive length change(%)	Mean slope(°)	Aspect
Xinqingfeng	1	G090837E36060N	1971-1987	278.4	17.4	2.3	13.5	N
			1989-1999	50.9	5.1	0.4		
	2	G090884E36076N	1987-1989	1200.0	600.0	7.8	9.2	NW
			1990-1998	256.0	32.0	1.7		
	4	G091032E36060N	2009-2016	1164.0	194.0	5.5	10.1	E
	6	G090901E36002N	2014-2016	46.0	23.0	0.4	17.7	S
	7	G090868E35998N	1986-1989	40.8	13.6	0.6	21.5	S
			2009-2010	107.8	107.8	1.6		
	8	G090846E36001N	1970-1986	663.0	41.4	11.5	21.9	S
Malan	14	G090693E35807N	2007-2012	260.5	52.1	2.8	7.6	S